Physical model inversion of the green spectral region to track assimilation rate in almond trees with an airborne nano-hyperspectral sensor

Suarez, L.[1*], González-Dugo, V.[2], Camino, C.[3], Zarco-Tejada, P.J.[1,2]

[1] School of Agriculture and Food, Faculty of Veterinary and Agricultural Sciences (FVAS), and Department of Infrastructure Engineering, Melbourne School of Engineering (MSE), University of Melbourne, Melbourne, Victoria, Australia. *E-mail: l.suarez@unimelb.edu.au

[2] Instituto de Agricultura Sostenible (IAS), Consejo Superior de Investigaciones Científicas (CSIC), Avenida Menéndez Pidal s/n, 14004 Córdoba, Spain

[3] European Commission (EC), Joint Research Centre (JRC), Ispra (VA), Italy

Highlights:

- Assimilation rate in orchards can be tracked with Vc_{max} derived from SCOPE model
- Best results are obtained using the green spectral region between 505 and 560 nm
- We show how traditional indices and methods are not providing universal links
- The method is consistent across phenological stages.

Keywords: Assimilation, photosynthesis, hyperspectral, radiative transfer model, RTM, SCOPE, Vc_{max}, green spectral región, fluorescence, SIF, PRI, Nano-Hyperspec.

Abstract

Significant advances toward the remote sensing of photosynthetic activity have been achieved in the last decades, including sensor design and radiative transfer model (RTM) development. Nevertheless, finding methods to accurately quantify carbon assimilation across species and spatial scales remains a challenge. Most methods are either empirical and not transferable across scales or can only be applied if highly complex input data are available. Under stress, the photosynthetic rate is limited by the maximum carboxylation rate (Vc_{max}), which is determined by the leaf biochemistry and the environmental conditions. Vc_{max} has been connected to plant photoprotective mechanisms, photosynthetic activity and chlorophyll fluorescence emission. Recent RTM developments such as the Soil-Canopy Observation of Photosynthesis and Energy fluxes (SCOPE) model allow the simulation of the sun-induced chlorophyll fluorescence (SIF) and Vc_{max} effects on the canopy spectrum. This development provides an approach to retrieve Vc_{max} through RTM model inversion and track assimilation rate. In this study we explore SIF, narrow-band indices and RTM inversion to track changes in photosynthetic efficiency as a function of vegetation stress. We use hyperspectral imagery acquired over an almond orchard under different management strategies which affected the assimilation rates measured in the field. Vc_{max} used as an indicator of assimilation was retrieved through SCOPE model inversion from pure-tree crown hyperspectral data. The relationships between field-measured assimilation rates and Vc_{max} retrieved from model inversion were higher (r^2= 0.7-0.8) than when SIF was used alone (r^2= 0.5-0.6) or when traditional vegetation indices were used (r^2=0.3-0.5). The method was proved successful when applied to two independent datasets acquired at two different dates throughout the season, ensuring its robustness and transferability. When applied to both dates simultaneously, the results showed a unique significant trend between the assimilation measured in the field and Vc_{max} derived using SCOPE (r^2=0.56, $p<0.001$). This work demonstrates that tracking assimilation in almond trees is feasible using hyperspectral imagery linked to radiative transfer-photosynthesis models.

1. Introduction

The accurate monitoring of plant photosynthetic activity at large scales is required to control the effects of potential threats affecting adequate growth and resulting yield (Kimball, 1983; Lobell *et al*., 2009; Long *et al*., 2015). Plants under water and nutrient stress regulate their photosynthetic rate reducing the production of assimilates (Schurr *et al*., 2006). Non-photochemical dissipation mechanisms protect the photosynthetic apparatus from excessive irradiance. These photoprotective mechanisms are very dynamic with illumination intensity and react within seconds or minutes (Demmig *et al*., 1987). The timely assessment of crop stress is therefore challenging as when symptoms are visually detectable, productivity and yield might be compromised (Hsiao *et al*., 1976; Hsiao and Bradford, 1983). In the particular case of orchards, in addition to frequent monitoring, the within-field heterogeneity resulting from changes in elevation, soil and irrigation system efficiency requires methods that properly assess the spatial variability of photosynthetic activity at the individual object level, e.g. at the tree scale. In the last decades, there has been an important advance towards developing remote sensing methods to detect pre-visual stress, that is before visual symptoms appear, and extend the assessment to describe within field variations (Chaerle, L., 2007; Suarez *et al*., 2009; Tremblay *et al*., 2011; Zarco-Tejada *et al*., 2012; Ihuoma and Madramootoo, 2017; Hernandez-Clemente *et al*., 2019).

Changes in both the green spectral region and in the emission of chlorophyll fluorescence from photosystem I (PS-I) and photosystem II (PS-II) have been connected to plant photosynthetic dynamic processes under stress (Papageorgiou, 1975; Gamon *et al*., 1992; Krause and Weis, 1991; Mohammed *et al*., 2019). The effect in the green region has been attributed to photoprotective mechanisms that dissipate part of the absorbed radiation under limited photosynthetic capacity, mainly through changes in xanthophyll pigment composition (Demmig-Adams, 1990). When incoming radiation exceeds the capacity of the photosynthetic reaction centres, the xanthophyll pigment violaxanthin (V) de-epoxidise to antheraxanthin (A) and later to

zeaxanthin (Z) to avoid oversaturation. This process has an effect on the spectral signal around 531 nm and has been used to track photosynthetic efficiency remotely (Gamon *et al*., 1992, Filella *et al*., 1996, Stylinski et al., 2000; Evain *et al*., 2004).

As a proxy of photosynthesis activity, the chlorophyll fluorescence signal can be quantified as the ratio between the maximum variable fluorescence emission to the maximum total fluorescence (Krause and Weis, 1991; Mohammed *et al*., 1995). The application of this method to image data is not practical though, being the focus on quantifying steady-state fluorescence signals, i.e. SIF, for the remote assessment. Among other methods, SIF can be quantified applying the Fraunhofer Line Depth (FLD) principle using the atmospheric O_2 absorption bands (Plascyk and Gabriel, 1975). Despite the high spectral resolution required to quantify fluorescence at the O_2-A and O_2-B absorption bands, modelling work by Damm *et al* (2011) demonstrated that sensors with 5-6 nm full-width at half maximum (FWHM) spectral bands within the oxygen absorption window can be used to derive sun-induced fluorescence through this method. As an example, Zarco-Tejada *et al*. (2012; 2016; 2018) and Damm *et al*. (2014; 2015a) showed successful retrievals of sun-induced fluorescence (SIF) using airborne sensors of such spectral characteristics in the context of stress detection, e.g. focusing on the relative spatial variability of SIF as an indicator of stress.

Although SIF has been demonstrated to be directly linked to photosynthetic activity (Mohammed et al., 2019; Meroni et al., 2009; Rascher et al., 2009; Zarco-Tejada et al., 2009), the amount of fluorescence emitted and its quantification based on the *in-filling* method described above is affected by the irradiance levels at the time of data acquisition, therefore highly variable in the temporal scale. Indices derived from the green region present similar issues when used with time series of image data (Gamon *et al*., 1997; Damm *et al*., 2015b). Attempts to normalise these indices calculated from reflectance and FLD methods with ancillary measurements have been frequent in the last years (Suarez *et al*., 2010; Zarco-Tejada *et al*., 2013b). Apart from the difficulties to properly normalise these spectral indices, the link between these indicators and

109 photosynthetic efficiency needs to be established to provide a meaningful interpretation (Nichol
110 *et al*., 2002; Running *et al*., 1999). This link is typically highly empirical, site and species specific
111 (Courault *et al*., 2005) and affected by structural and pigment levels across species.

112 The estimation of photosynthetic parameters (i.e. Vc_{max}) is an alternative approach that does not
113 rely on further empirical links. The limitation in the enzyme kinetic processes driving
114 photosynthesis is defined by two parameters, the maximum electron transport rate (J_{max}) and the
115 maximum carboxylation rate (Vc_{max}) by the Ribulose-1,5-bisphosphate carboxylase/oxygenase
116 (RuBisCO) enzyme under saturated light conditions. Both Vc_{max} and J_{max} change in response to
117 environmental conditions and the CO_2 fixation rate is determined by the most limiting of them
118 (Farquhar *et al*., 1980). Vc_{max} has been proposed as a useful parameter linked to photosynthetic
119 rate, given its responsiveness to biotic and abiotic stressors, such as insect or pathogen damage
120 (Dungan *et al*., 2007) and drought (Xu and Baldocchi, 2003). In the field, Vc_{max} is obtained from
121 leaf measurements made with a gas exchange instrument using net assimilation of CO_2–
122 intercellular CO_2 concentration (A–Ci) curves (Farquhar *et al*., 1980). However, measuring Vc_{max}
123 on the ground is time-consuming and logistically impossible for timely large-area assessments of
124 the natural heterogeneity present in agricultural fields.

125 Empirical models derived by Serbin *et al.* (2012, 2015) showed there is a strong spectral response
126 to Vc_{max} changes in the blue-green and the Red-Edge spectral regions but reached the conclusion
127 that there is not unique link between spectral signal and Vc_{max} and the large-area assessment of
128 Vc_{max} based on spectral data needed to account for species type and environmental factors at the
129 time of image acquisition. Recent advances in physical models have linked the radiative transfer
130 theory with plant physiological modules where photosynthetic performance can be simulated as
131 a function of stress and environmental conditions (Van der Tol *et al*., 2009). This is the case of
132 the Soil Canopy Observation, Photochemistry and Energy fluxes model (SCOPE, Van der Tol *et*
133 *al*., 2009). The SCOPE model allows the simulation of the effect of varying Vc_{max} on the canopy

spectra including the emission as fluorescence. According to model simulations, these effects are spectrally located in the green (505 – 560 nm) and in the red and far-red chlorophyll fluorescence emission (650 - 850 nm) regions. By establishing the physical link between the spectral signal and Vc_{max}, changes in photosynthetic activity can be tracked without relying on site specific empirical relationships.

With the recent progress on the estimation of SIF at the global scale (Frankenberg *et al*., 2011; Guanter *et al*., 2014), especial interest has been put on models such as SCOPE for carbon accounting (Koffi *et al*., 2015). Some studies have demonstrated the big potential of SCOPE in combination with satellite-derived SIF to monitor carbon sequestration against international agreement targets (Zhang *et al*., 2014; Guan *et al*., 2016), although the spatial resolution of SIF derived from satellite imagery poses many challenges related to pixel heterogeneity and ancillary input data availability (Verma *et al*., 2017) which makes its interpretation complex. These challenges could be overcome by increasing the model capabilities to properly simulate the within-pixel heterogeneity. Increasing image spatial resolution to minimise the effect of mixed scene elements is another potential solution.

At the finer scale and in the context of precision agriculture, the assessment of Vc_{max} through physical models might provide an advantage for the quantitative monitoring of canopy assimilation over time without relying on empirical methods that are not robust across scales and environmental conditions. As a photosynthetic trait, Vc_{max} does not require any further link or empirical calculation to track assimilation over time. As an example, Camino *et al*. (2019) demonstrated the retrieval of Vc_{mo} (e.g. Vc_{max} of a top leaf standardised to a reference temperature at 25 °C) through SCOPE radiative transfer model inversion to track photosynthetic rate differences in wheat under nutrient and water stress.

157 The SCOPE model simulates the canopy as a 1D homogeneous flat turbid medium (Van der Tol
158 *et al*., 2009; Verhoef, 1984). This arrangement is ideal to simulate continuous crops like wheat
159 but might be limited when attempting the same with discontinuous woody vegetation structures.
160 Heterogeneous canopy scenes (i.e. tree orchards) present a complex arrangement of canopy,
161 sunlit soil background and shadows (Verstraete *et al*., 1990; Law *et al*., 2001) adding complexity
162 to the simulation of the multiple scattering effects between the different elements (Widlowski *et*
163 *al*., 2006). Submeter spatial resolution imagery allows the extraction of pure crown pixels avoiding
164 shadows and the tree crown edges that are more exposed to horizontal fluxes, therefore
165 minimizing the effects of the canopy discontinuity. However, modeling the within-crown structural
166 parameters remains a challenge when simulating tree crowns as a turbid medium. It has been
167 demonstrated that the shaded gaps and the signal and angular arrangement of the different
168 canopy elements including branches and twigs play an important role on the overall reflectance
169 signal (Cescatti, 1997; Verrelst *et al*., 2010). Regardless the limitations, 1D models have been
170 successfully inverted to retrieve complex canopy properties in the past (see Jacquemoud *et al*.
171 (2009) for a review).

172 Here we show how SCOPE model inversion can be used to track photosynthetic activity in an
173 almond tree orchard using high spatial resolution imagery collected with an airborne lightweight
174 hyperspectral sensor. Although both the green and the red-far red spectral regions are explored,
175 we show the potential of the green region to invert Vc_{max} for photosynthetic rate monitoring. The
176 validity of the method is tested for independent datasets acquired at different phenological stages.

177

2. Materials and methods

2.1. Study site and experimental field

The study site is an almond orchard (cv. Guara onto GF-677 rootstock) located in Cordoba Spain (37°52′N, 4°49 W) growing under a Mediterranean weather characterized by warm and dry summers, cold and wet winters and an annual rainfall around 550 mm, mainly occurring in Spring and Autumn. The orchard was established in 2009 on a sandy loam soil in a 6 x 7 m grid, resulting in a tree density of 238 trees per ha.

During three years, four replicates of three different water and nutrient management treatments were applied to plots of 16 trees resulting in a wide range of stress variability. The first treatment, which trees were considered as control, was fertilized and irrigated to satisfy full requirements calculated following Fereres *et al*. (2012). The other two treatments followed a regulated deficit irrigation scheme (RDI), receiving 20% of full water requirements during kernel filling and 60% of control rates after harvest. The first of the RDI treatments received the same amount of N as the control treatment, fertilization rate of the second RDI was reduced to a 75% of the control. All trees were kept free of weeds, and pests and diseases were fully controlled. Table 1 gives an overview of the different treatments applied and a full description of the experimental site can be found in Espadafor *et al*. (2017) and Lopez-Lopez *et al*. (2018).

Table 1. Summary of irrigation and fertilization treatments applied in the experimental site.

Treatment	**Irrigation**	**Fertilisation**
Treatment 1: Control	Full ET	100% N
Treatment 2: RDI 1	Regulated Deficit Irrigation: - 20% full ET during kernel filling - 60% after harvest	100% N
Treatment 3: RDI 2	Regulated Deficit Irrigation: - 20% full ET during kernel filling 60% after harvest	75% N

197 During the growing season, two central trees of each plot were monitored. Data collection
198 included assimilation rate using a portable photosynthesis system (LCDpro-SD, ADC,
199 Bioscientific Ltd., Herts, UK) and stomatal conductance with a porometer device (SC-1, Decagon
200 Devices Inc., Pullman, WA, USA) both measured on two to four leaves per tree. Chlorophyll
201 concentration was measured on 10 to 15 leaves using a SPAD meter (SPAD502DL, Minolta,
202 Japan) and leaf steady-state fluorescence with a pulse amplitude modulated fluorometer
203 (Fluorpen FP110, Photon Systems Instruments, Brno, Czeck Republic) on 10 leaves per tree.

204

205 **2.2. Field data collection and airborne campaigns**

206 Two airborne campaigns were conducted using a nano-hyperspectral imager (Headwall
207 Photonics, Fitchburg, MA, USA) on DOY: 218 and DOY: 237 (summer, 2015) corresponding to
208 the kernel filling period and after harvest respectively. Flight design and airborne operations were
209 coordinated by the Laboratory for Research Methods in Quantitative Remote Sensing
210 (QuantaLab) of the Spanish Council for Scientific Research (IAS-CSIC, Córdoba, Spain). The
211 specifications of the nano-hyperspectral imager used are detailed in Table 2. Flying operation
212 was carried out on the solar principal plane at 250 m above ground level with a speed of 130
213 km/h, yielding a ground spatial resolution of 30 cm. Within 3 days of the image acquisition, a field
214 dataset was collected by sampling two central trees of each treatment block as described above.

215 The imagery was radiometrically calibrated keeping the original instrument FWHM of 6.5nm.
216 Image raw data were transformed into radiance using calibration coefficients derived from
217 measurements against a calibration standard (CSTM-USS-2000C LabSphere, North Sutton, NH,
218 USA) at four integration times over four illumination intensities. The image atmospheric correction
219 was conducted with SMARTS model (Gueymard 1995, 2001) using aerosol optical parameters
220 measured with a handheld sun-photometer (Microtops II, Solar Light Co., Philadelphia, PA, USA)

and air temperature, relative humidity and air mass measured with a portable weather station (WX510 from Vaisala, Vantaa, Finland).

Irradiance was also measured in the field with a cosine receptor unit attached to an upward looking spectrometer covering the 350-2500 nm spectral range (Fieldspec III Pro, Analytical Spectral Devices, Inc., Malvern Panalytical). This field measured irradiance was later used as input in the model simulations. Ortho-rectification of each single hyperspectral flightline was performed using PARGE software package (ReSe Applications Schläpfer, Wil, Switzerland) based on the readings of an Inertial Measuring Unit (IMU) installed on-board the airborne platform during the flight.

The pixels corresponding to each individual tree crown in the orchard were selected using an automated process as reported in Calderon *et al*. (2015), ensuring only pure vegetation pixels were considered for the analysis. Figure 1c presents an example of reflectance and radiance resulting from the segmentation for one tree crown from a control plot together with the irradiance measured at the time of the image acquisition. Figure 2 shows the average reflectance and radiance spectra for the different treatments.

Table 2. Platform and sensor operational settings during image acquisition

Hyperspectral sensor characteristics and settings	
Spectral range (nm)	400 – 885
Number of spectral bands	260
FWHM	6.5 nm
Slit size	25 μm
Detector pixel pitch	7.4 μm
Focal length	4.8 mm
Radiometric resolution (bits)	12
Integration time	18 ms
Image acquisition details	
Acquisition dates and times	6th & 25th August 2015, solar noon
Flying height (AGL)	250 m
Cruise speed	130 km/h
Mean spatial resolution (m)	0.3

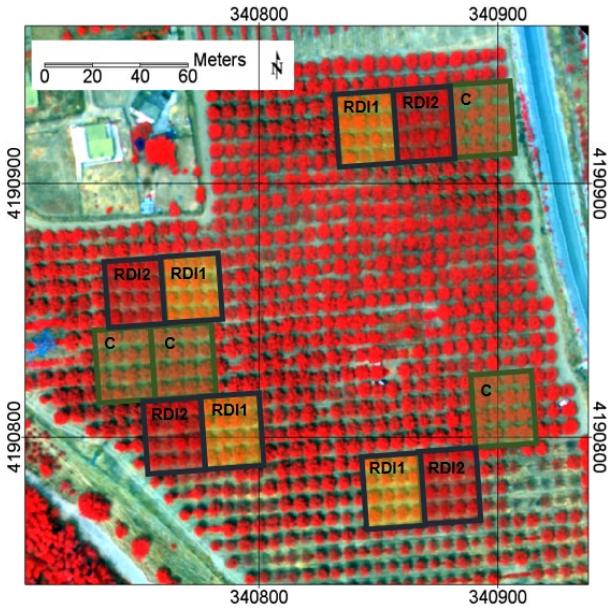

(a)

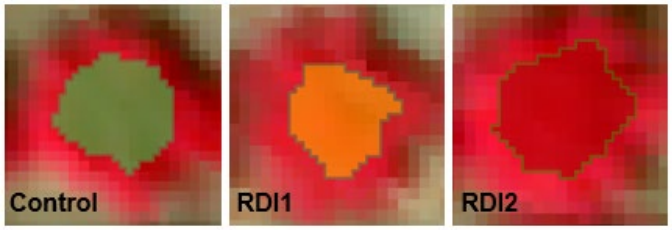

(b)

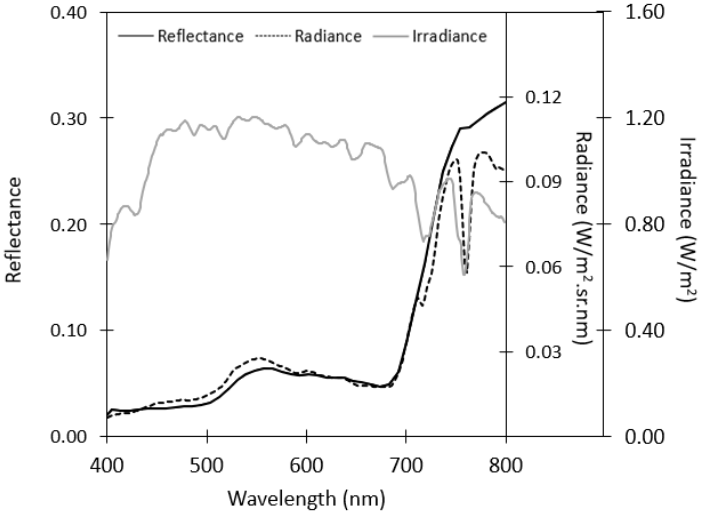

(c)

Figure 1. Overview of the image captured over the experimental field on DOY 160 (a) with the control blocks in green (C), RD1 blocks in yellow and RD2 blocks in red. Zoom of the automatic segmentation applied to one tree of each treatment (b), example reflectance and radiance spectrum from a tree of the control group (c).

Spectral indices traditionally used for vegetation stress detection were calculated using the average value of the reflectance spectra extracted from each tree crown in the experiment (Table 3). The index selection comprises structural indices typically related to vigour and foliage density, indices used to assess pigment concentration and special attention was put on stress indices calculated from the green spectral region due to their connection to photoprotective processes under water and nutrient stress conditions. Sun induced fluorescence was also retrieved from the hyperspectral imagery using the FLD principle applied to the O_2-A absorption line at 760 nm. The method was applied to the image data using the bands at 762nm and 750 nm as the centre of the absorption feature and reference radiance, respectively (Table 3).

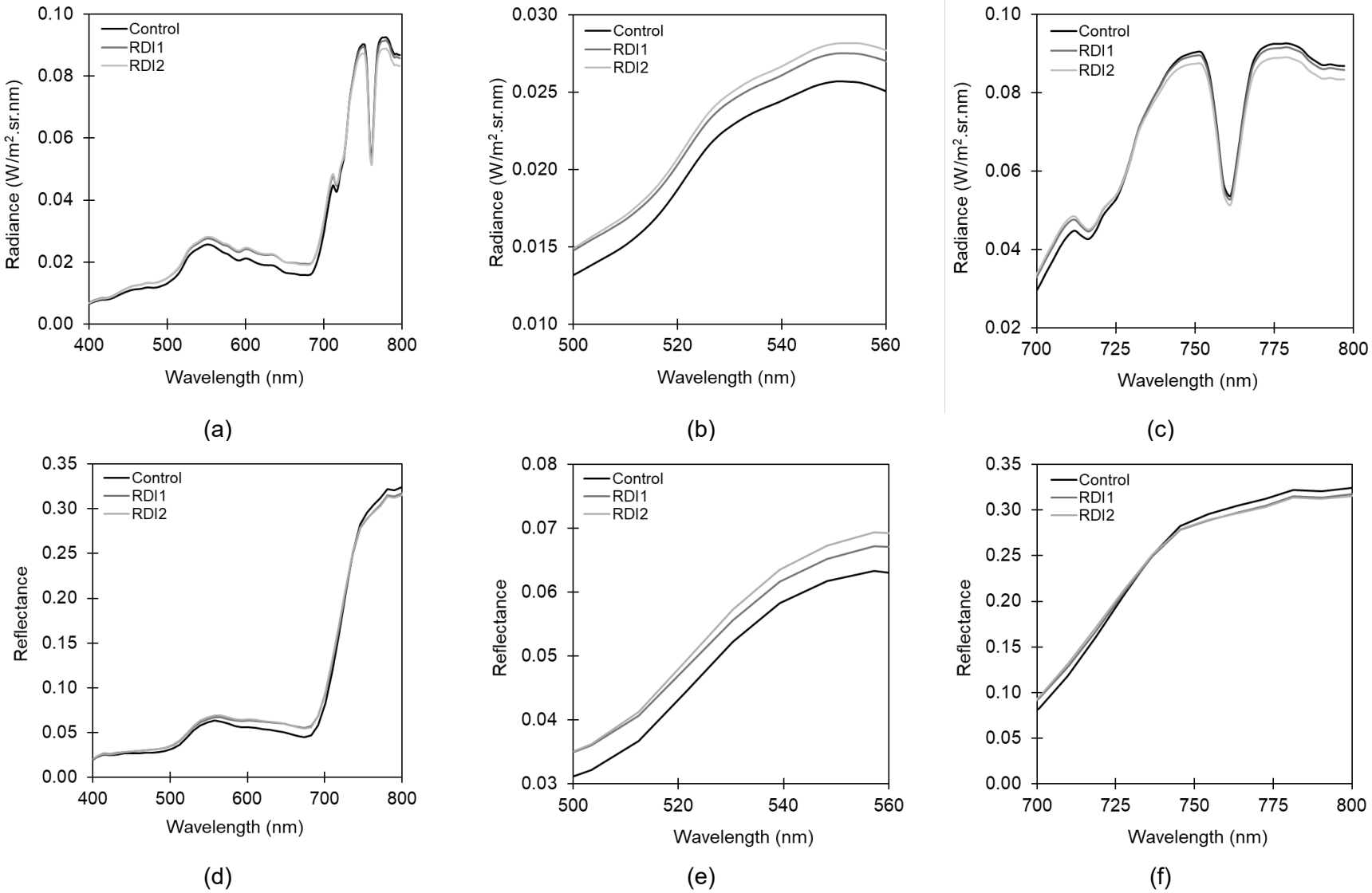

Figure 2. Average radiance and reflectance spectrum for each of the treatments over the 400-800nm spectral range (a and d), zooms over the green (500-560 nm) region (b and e) and far-red-NIR (700-800 nm) region (c and f) where physical models indicate Vc_{max} change effects.

Table 3. List of spectral indices used in the study with their formulation and original reference. R_λ, L_λ and E_λ refers to reflectance, radiance and irradiance at λ nm.

Index	Formulation	Reference
Structural indices		
NDVI	$(R_{800} - R_{670}) / (R_{800} + R_{670})$	Rouse *et al*. (1974)
RDVI	$(R_{800} - R_{670}) / (R_{800} + R_{670})^{0.5}$	Rougean and Breon (1995)
EVI	$2.5 \cdot (R_{800} - R_{670}) / (R_{800} + 6 \cdot R_{670} - 7.5 \cdot R_{400} + 1)$	Huete *et al*. (2002)
MTVI	$1.2 \cdot (1.2 \cdot (R_{800} - R_{550}) - 2.5 \cdot (R_{670} - R_{550}))$	Broge & Leblanc (2000); Haboudane *et al*. (2004)
Chlorophyll indices		
CI	R_{750} / R_{710}	Zarco-Tejada *et al*. (2001)
TCARI/OSAVI	$3 \cdot ((R_{700} - R_{670}) - 0.2 \cdot (R_{700} - R_{550}) \cdot (R_{700} / R_{670})) / ((1 + 0.16) \cdot (R_{800} - R_{670}) / (R_{800} + R_{670} + 0.16))$	Haboudane *et al*. (2002)
SIPI	$(R_{800} - R_{445}) / (R_{800} + R_{680})$	Peñuelas *et al*. (1995)
Xanthophyll-related Indices in the green region		
PRI	$(R_{570} - R_{530}) / (R_{570} + R_{530})$	Gamon *et al*. (1992)
PRI_{515}	$(R_{515} - R_{530}) / (R_{515} + R_{530})$	Stagakis *et al*. (2012)
PRI_{M1}	$(R_{512} - R_{531}) / (R_{512} + R_{531})$	Gamon *et al*. (1993)
PRI_{M2}	$(R_{600} - R_{531}) / (R_{600} + R_{531})$	Gamon *et al*. (1993)
PRI_{M3}	$(R_{670} - R_{531}) / (R_{670} + R_{531})$	Gamon *et al*. (1993)
PRI_n	$PRI / [RDVI \cdot (R_{700} / R_{670})]$	Zarco-Tejada *et al*. (2013)
Fluorescence quantification		
Fraunhofer Line Depth (FLD)	$FLD = ((E_{750} \cdot L_{762}) - (E_{762} \cdot L_{750})) / (E_{750} - E_{762})$	Plascyk and Gabriel (1975)

All spectral indices including FLD as an indicator of sun-induced fluorescence were computed using the average reflectance and radiance extracted from each tree crown, being the tree crown our individual object of study. Linear interpolation was used to derive the reflectance value corresponding to each band in the formulas.

2.3. Simulation of Vc_{max} spectral effects with SCOPE model

The SCOPE (Van der Tol *et al*., 2009) radiative transfer model was used to simulate the effects of the photosynthetic performance changes on the canopy spectral signal, including the emitted chlorophyll fluorescence. SCOPE model incorporates the influence of photosynthetic activity processes into a coupled leaf-canopy radiative transfer model resulting in a tool to study the effect

of vegetation stress on the canopy reflectance. The leaf radiative transfer module is based on FLUSPECT leaf model (Vilfan *et al*., 2016) which simulates leaf reflectance using leaf thickness, dry matter and water content, chlorophyll, anthocyanin and carotenoid content. To incorporate the Vc_{max} and J_{max} rates driving the RuBisCO enzyme activity in the photosynthetic process, the SCOPE model uses the Farquhar–von Caemmerer–Berry (FvCB; Farquhar *et al*. (1980)) photosynthesis model, the stomatal resistance (Cowan, 1978), the Ball–Berry stomatal conductance model (Ball *et al*., 1987) and the coupled photosynthesis-stomatal model by Collatz *et al*. (1991). Vc_{max} and J_{max} determine the maximum carboxylation rate of RuBisCO and the maximum rate of photosynthetic electron transport varying in response to environmental conditions and governing the potential assimilation rate. J_{max} has been demonstrated to vary linearly with Vc_{max} as function of air temperature (Woodward *et al*., 1995). The fluorescence and energy balance modules in SCOPE incorporate the effects of Vc_{max} changes in the radiative transfer equation returning the overall canopy signal function of stress (Van der Tol *et al*., 2014). During its execution, the model ensures the energy balance closure integrating the thermal radiation, environmental conditions, leaf biochemistry and chlorophyll fluorescence and canopy radiative transfer (Van der Tol *et al*., 2009).

The SCOPE model input to track Vc_{max} is the maximum carboxylation rate of a top leaf standardized to a reference temperature at 25°C (Vc_{mo}). We will refer to it as Vc_{max} from now onwards for easiness, and considering the air temperature at the time of image acquisition was within 5 degrees of the optimal 25°C. The spectral effects resulting from varying Vc_{max} can be seen Figure 3, which shows the simulated spectra for Vc_{max} changing from 0 to 250 μmol m^{-2} s^{-1} using a standard set of input values and the ambient conditions at the time of DOY 237 airborne data collection. The effect on the signal is very subtle (dotted line, Figures 3a-c) concentrated in the green region (505-560 nm) and in PS-I and PS-II chlorophyll fluorescence emission regions (650 – 800 nm). Figures 3b and 3c show a zoom over the areas where this effect is observed. The same effects on the chlorophyll fluorescence emission region where reported by Zarco-

Tejada *et al*. (2013a) using FluorSAIL radiative transfer model (Verhoef, 2005) coupled to FLIM (Rosema *et al*., 1992) developing the FluorFLIM hybrid model.

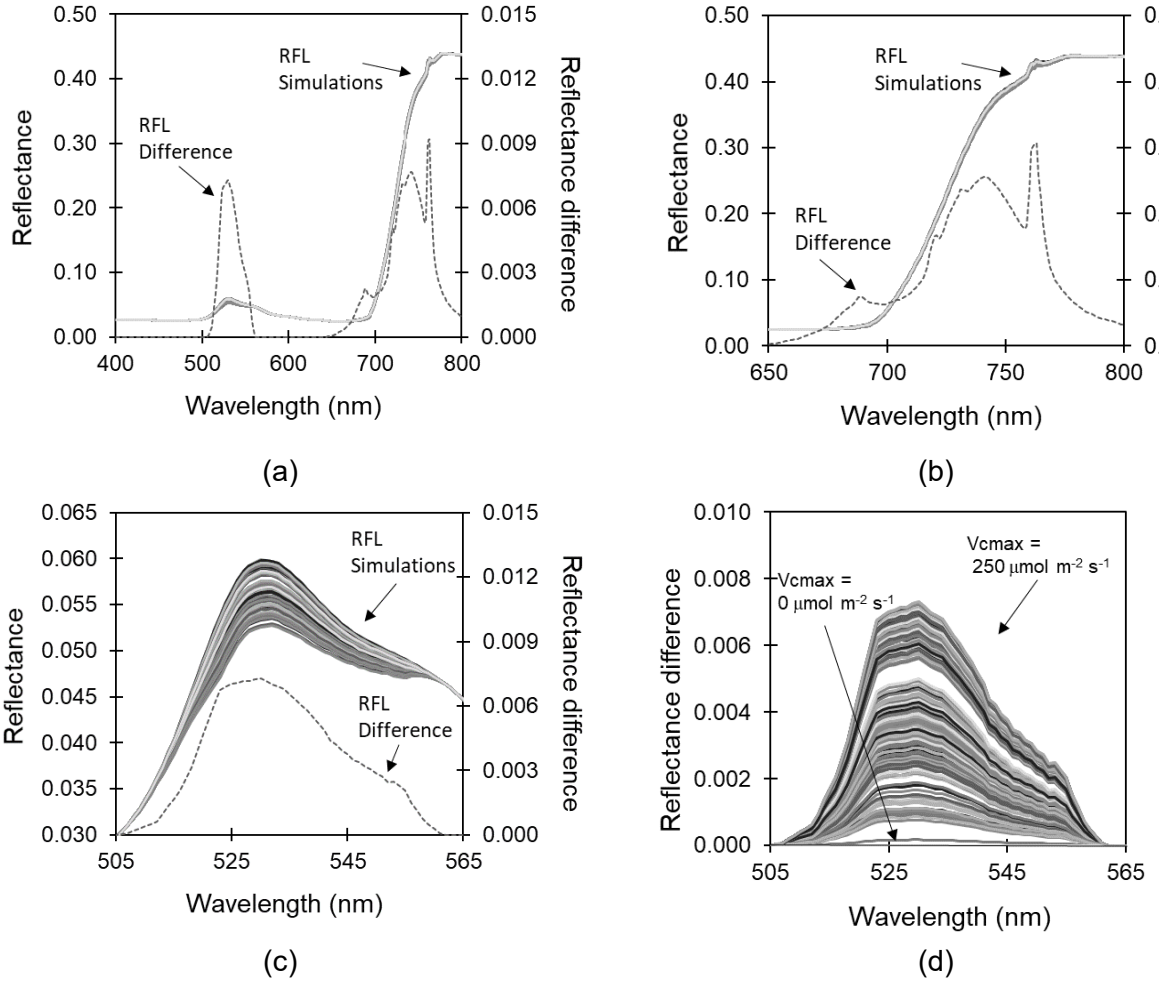

Figure 3. Results of simulating the spectral response to Vc_{max} variation over the range 10 to 250 μmol m^{-2} s^{-1} leaving the rest of parameters fixed (LAI=3, Cab=80, Cm=Cw=0.02) for the full 400-800nm range (a), for the 650-800nm region (b) and for 505-565 nm region (c). Reflectance difference between the maximum and minimum feature result of Vc_{max} variation is represented in a dotted line. (d) reflectance difference represented for 200 simulations with Vc_{max} ranging from 0 to 250 μmol m^{-2} s^{-1} over the green spectral feature.

The absolute reflectance difference resulting from Vc_{max} variation from 0 to 250 μmol.m^{-2}.s^{-1} has similar dimensions in both the green and the fluorescence emission region (Figure 3a, dotted line). The reflectance difference to reflectance signal ratio is therefore up to ten times higher in the green region than in the NIR as the reflectance in the visible is much lower as a result of

pigment absorption. Figure 3d represents the family of 200 simulations with Vc_{max} ranging from 0 to 250 μmol/m^2·s in the green region.

SCOPE simulations were also used to investigate potential relationships between Vc_{max} and existing indices in the green region (i.e. the Photochemical Reflectance Index (PRI), Gamon *et al*. (1992) and the family of formulations derived from PRI in Table 3) and SIF@760 quantified through the FLD method. Vc_{max} vs PRI and Vc_{max} vs SIF were investigated for chlorophyll content between 20 and 70 μg/cm^2 and for changes in LAI 1-2 to assess the potential of establishing links between vegetation indices and Vc_{max} that are robust to variations in pigment content and vigour.

2.4. SCOPE model inversion for Vc_{max} estimation

SCOPE model was inverted to retrieve Vc_{max} as a proxy of assimilation rate for every tree in the experimental field acquired by the hyperspectral imager at the two acquisition dates. Inversions were carried out using pure vegetation pixels extracted without edge effects, as described previously. The model inversion was conducted based on the local spectral signal variations in the green (505-560 nm, as shown in Figure 3c) and red-far red (690-750 nm, Figure 3b) regions. In addition to using each region independently, the analysis also comprised both regions together and the full spectrum from 500 to 750nm. Figure 4 presents an overview of the steps followed to retrieve Vc_{max} through model inversion.

Simulations were carried out with the atmospheric and background input parameters fixed according to known data or measurements on the image acquisition day. That includes location and sensor geometry, irradiance at the time of the flight, meteorological parameters and the soil reflectance. The irradiance used in the atmospheric module of SCOPE corresponded to the field-measured irradiance, while the direct and diffuse components were calculated to keep the modelled proportional contribution. Once the irradiance was set to the field-measured spectra, the incoming shortwave radiation (R_{in}) input was adjusted to match the simulated radiance with

the image radiance levels. As most of the canopy spectrum over the visible and NIR is the result of structure and pigment concentration, *ill-posed* solutions are frequent when those inputs are not well constraint and the parameter of interest has a comparatively small effect on the signal (Combal *et al*., 2003, Atzberger and Richter, 2012). Consequently, a multi-step inversion approach (Combal *et al*., 2001; Atzberger, 2004; Laurent *et al*., 2014) was adopted to estimate Vc_{max}. First, model input parameters were constrained to specific ranges to avoid potential *ill-posed* inversion solutions. The ranges were established based on field measurements, existing literature and preliminary model simulations to make sure the resulting look-up-table (LUT) covered the tree crown spectral range of variability.

Under the assumption that in a well-managed orchard most structural properties present limited variation, the first inversions focused on fixing the ranges for the leaf structural parameter N and the leaf area index (LAI). Leaf orientation function was left to vary as it was demonstrated that almond trees adjust the leaf exposure to incoming illumination as function of stress (Egea *et al*., 2012). Leaf dry matter and water content are typically only affected after long term stress. In this case, they were also left to fully vary to consider the potential effect of long-term running treatments on the trees. Where there was not prior information or measurements, default values suggested for SCOPE model were used. Once the input ranges were established, the LUT was built by simulating a combination of random variations of the input values within the selected ranges. Table 4 shows the final input parameter ranges used to build the LUTs to invert Vc_{max} for each image acquisition date. All simulations were convolved to the wavelength range, spectral sampling interval and FWHM of the nano-hyperspectral imager used in this study. The convolution was carried out assuming gaussian band spectral response functions of 6.5 nm FWHM centered at the imager band locations. After applying the spectral convolution to the simulated reflectance, both simulations and imagery spectral dataset were comparable to execute the inversion.

In order to remove data noise affecting model inversion and considering the bell-shaped response of changes in Vc_{max} as opposed to narrow spectral features (Figure 3), further smoothing of the

data was applied using a low-degree polynomial filter (Savitzky and Golay, 1964). The Savitzky-Golay filter was applied to the data on the whole spectral range avoiding the region between 745 and 775 nm to avoid an impact on the O_2-A absorption region at 760 nm. For both simulations and image data, the amplitude of the second degree gaussian wavelet transformation was computed over four spectral ranges: i) 505 – 560 nm; ii) 690 – 750 nm, iii) the combination of both; and iv) the full 500 – 750nm range. Vc_{max} was estimated for each tree crown as the LUT entry with closest wavelet transformed spectrum using the root mean square error as cost function [1]. The rest of the input parameters derived for each tree crown were used for verification purposes only (e.g. to validate the consistency of the results over time).

$$RMSE = \sqrt{\sum_{\lambda i}^{\lambda j} \frac{(\,RFL_{obs}(\lambda) - RFL_{sim}(\lambda)\,)^2}{N}} \qquad [1]$$

Where λ_i and λ_j are the initial and end band of the spectral range, N is the total number of bands and $RFL_{obs}(\lambda)$ and $RFL_{sim}(\lambda)$ are the reflectance spectra from the image and from the model simulations, respectively, at a specific wavelength.

Similar method was applied by Kattenborn *et al*. (2017) to derive plant traits from airborne hyperspectral imagery. The only adaptation made in this study was to include only 3 scales in the wavelet transformation. The reason to use less scales was to adjust the width of the wavelets to inform the changes over smaller spectral regions as opposed to characterising the effects over the full visible-NIR spectral signal. Artifacts resulting from potential signal noise on those spectral regions were removed after applying the smoothing filter. A lower filter size was applied to the red-far red region to avoid the elimination of narrow spectral effects.

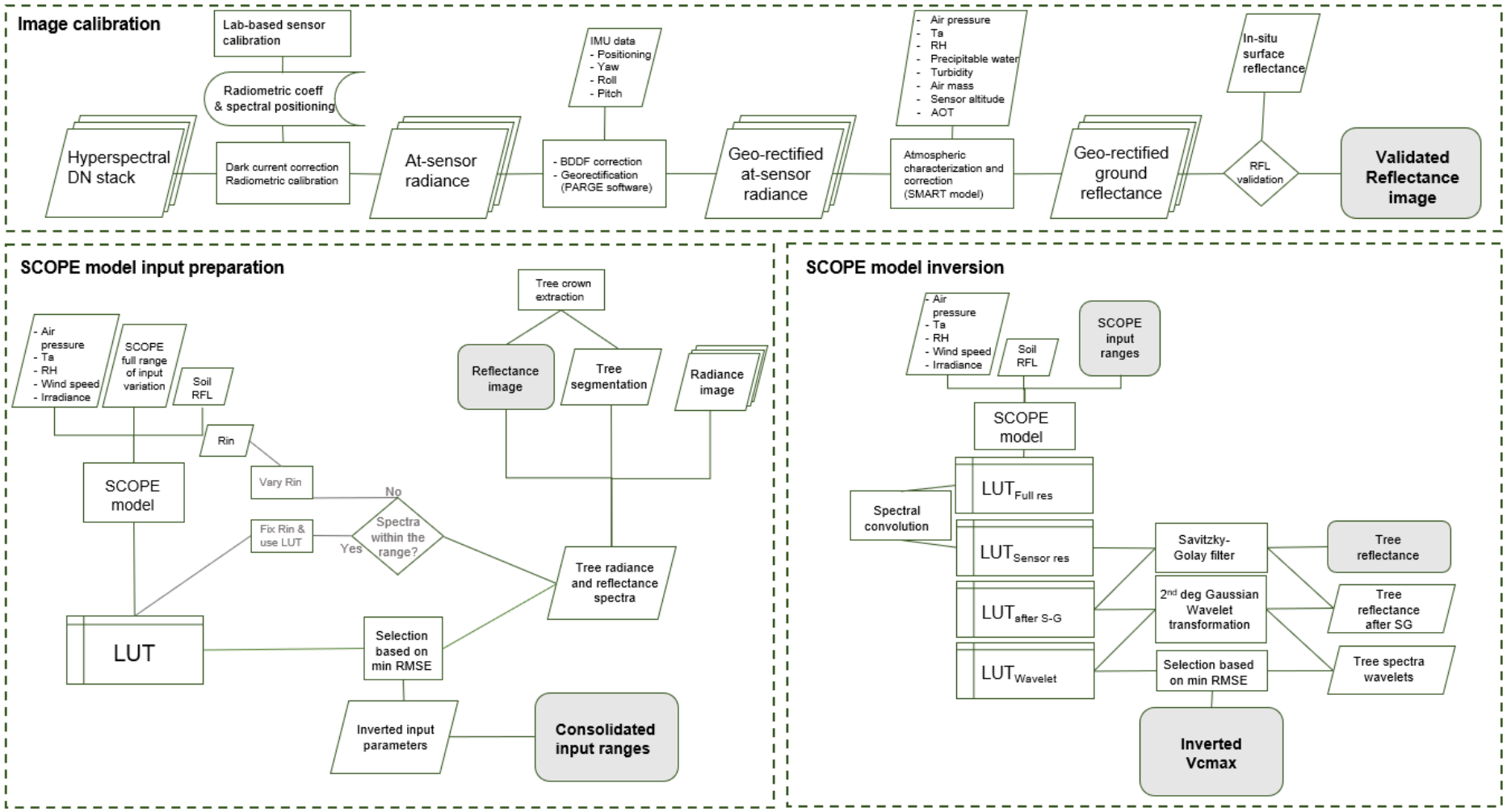

372

373 Figure 4. Overview of the methodology used to retrieve Vc_{max} through SCOPE model inversion including hyperspectral image calibration,
374 SCOPE parametrisation and input preparation and SCOPE model inversion.

375

376 Table 4. Input units and intervals used for SCOPE model inversion.

Parameter	Definition	Unit	Range / Value
Leaf biophysical parameters			
N	Leaf structural parameter	[-]	1.7 - 1.9
C_{ab}	Chlorophyll a & b content	$\mu g/cm^2$	35 - 60
C_{car}	Carotene content	$\mu g/cm^2$	6 - 18
C_{ant}	Anthocyanin content	$\mu g/cm^2$	0 - 8
C_w	Leaf water content	g/cm^2	0.001 - 0.05
C_m	Leaf dry matter content	g/cm^2	0.001 - 0.05
C_s	Brown pigment content	$\mu g/cm^{-2}$	0
lw	Leaf width	m	0.07
Leaf biochemistry			
Vc_{max}	Maximum carboxylation rate	$\mu mol/m^2 \cdot s$	30 – 110
m	Ball-Berry stomata conductance	[-]	8
Rd_{param}	Dark respiration	[-]	0.015
K_v	Vertical profile of Vc_{max} extinction coefficient	[-]	0.64
K_c	Cowan's water use efficiency	[-]	700
T	Temperature sensitivity parameters for Vc_{max} and Resp	[-]	0.2, 0.3, 283, 311, 328
ρ(thermal)	Leaf reflectance in thermal region	[-]	0.01
τ(thermal)	Leaf transmittance in thermal region	[-]	0.01
ρ_s(thermal)	Soil reflectance in thermal region	[-]	0.06
Stressfactor		[-]	1
f_{qe}	Fraction of photons partitioned to PSII	[-]	0.02
Canopy parameters			
LAI	Leaf area index	m^2 / m^2	0.5 – 2.3
$LIDF_a$	Leaf Inclination Distribution Function parameter a	[-]	-0.5 – 0.5
$LIDF_b$	Leaf Inclination Distribution Function parameter b	[-]	-0.5 – 0.5
Micrometeorological			
p	Air pressure	hPa	1010
u	Wind speed	m/s	1.6
O_a	O2 concentration in the air	ppm	209
ea	Atmospheric vapour pressure	hPa	0.15
C_a	CO2 concentration in the air	ppm	380
T_a	Air temperature	ºC	30
R_{in}	Incoming shortwave radiation	W/m^2	700
R_{li}	Incoming longwave radiation	W/m^2	300

377

3. Results

3.1 Field measurements

Physiological measurements collected in the field at the time of the image acquisitions depicted the stress variability consequence of the different water and nutrient management treatments. The ranges of variation of the leaf data collected on the whole experiment are shown in Figure 5.

Leaf assimilation rates varied from 1.2 to 16.2 μmol m^{-2} s^{-1} for all the leaves measured. The measurements were averaged per tree and later per treatment plot (2 trees per plot) for a total of 4 repetitions per treatment. Averaged plot values were used for further analysis. The ranges of variation found for the rest of the leaf parameters measured in the field can be found in Figures 5b-d.

The impact of varying LAI and chlorophyll content on the spectra, and therefore on the relationships Vc_{max} vs. PRI and Vc_{max} vs. SIF was further investigated using SCOPE simulations. Figure 6 shows there is not a single relationship for Vc_{max} estimation using PRI or SIF as the relationship is highly affected by the canopy structure (i.e. LAI; Figures 6a and 6b) and chlorophyll content (Figures 6c and 6d). Similar results were obtained for other indices of the PRI family developed to account for the effects of canopy structure or pigment concentration (data not shown).

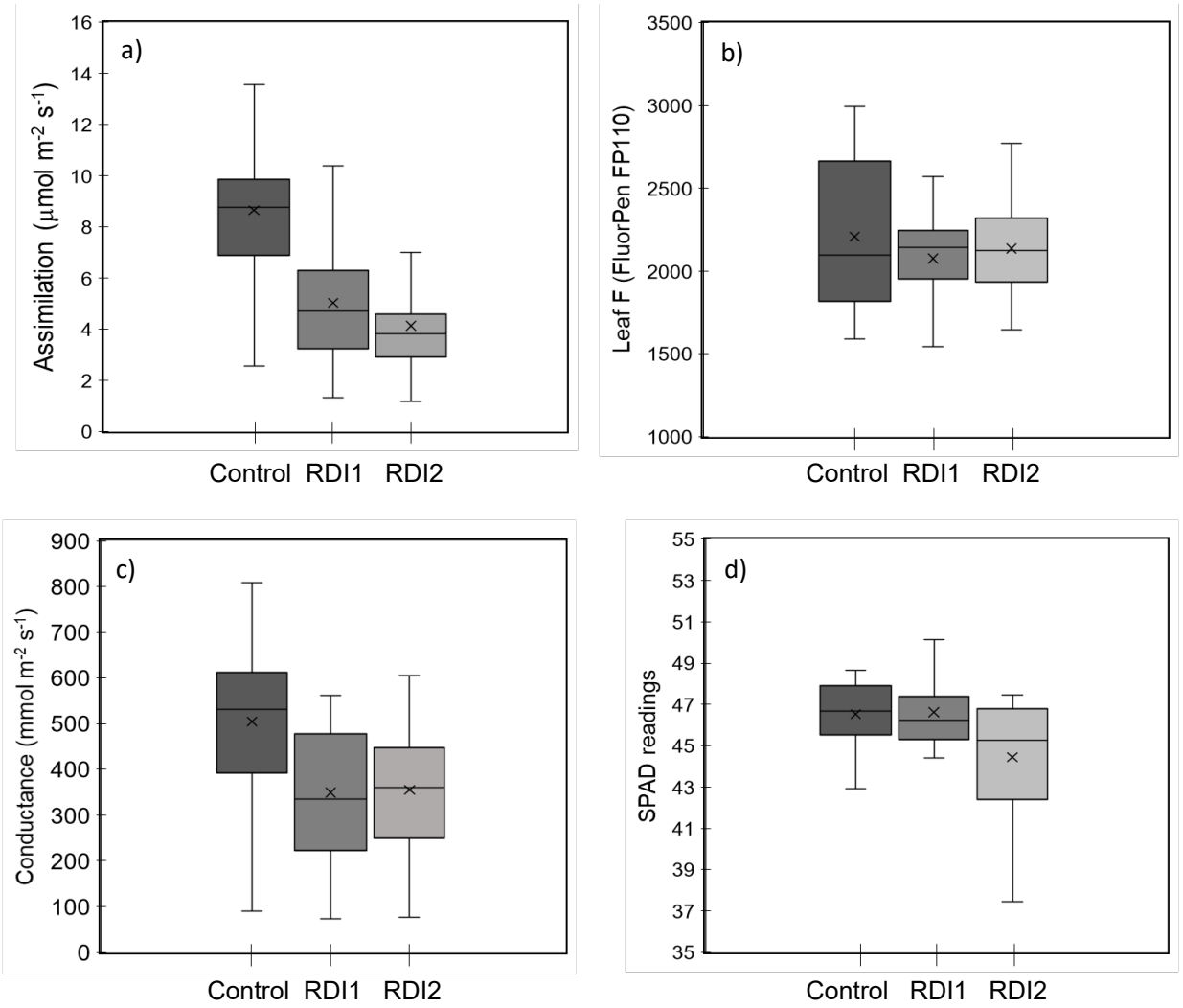

Figure 5. Ranges of variation for the four physiological variables measured in the field at both dates: Assimilation rate (a), stomata conductance (b), steady-state fluorescence (c) and SPAD chlorophyll index (d). Crossing line refers to median value and box amplitude refers to the second and third quartiles' limits. Whiskers represent the max and minimum data without outliers.

3.2. SCOPE model inversion for Vc_{max} estimation

The lack of a single relationship between modelled Vc_{max} and PRI, highly affected by structure and chlorophyll content, explains why the coefficients of determination and significance of the relationships between reflectance indices calculated from the hyperspectral imagery and the field-measured assimilation rate for each day are not very strong, ranging between r^2=0.04 and r^2=0.47. Still, indices in the green region and FLD as a proxy of SIF outperformed structural and pigment indices when tracking assimilation levels (Table 5).

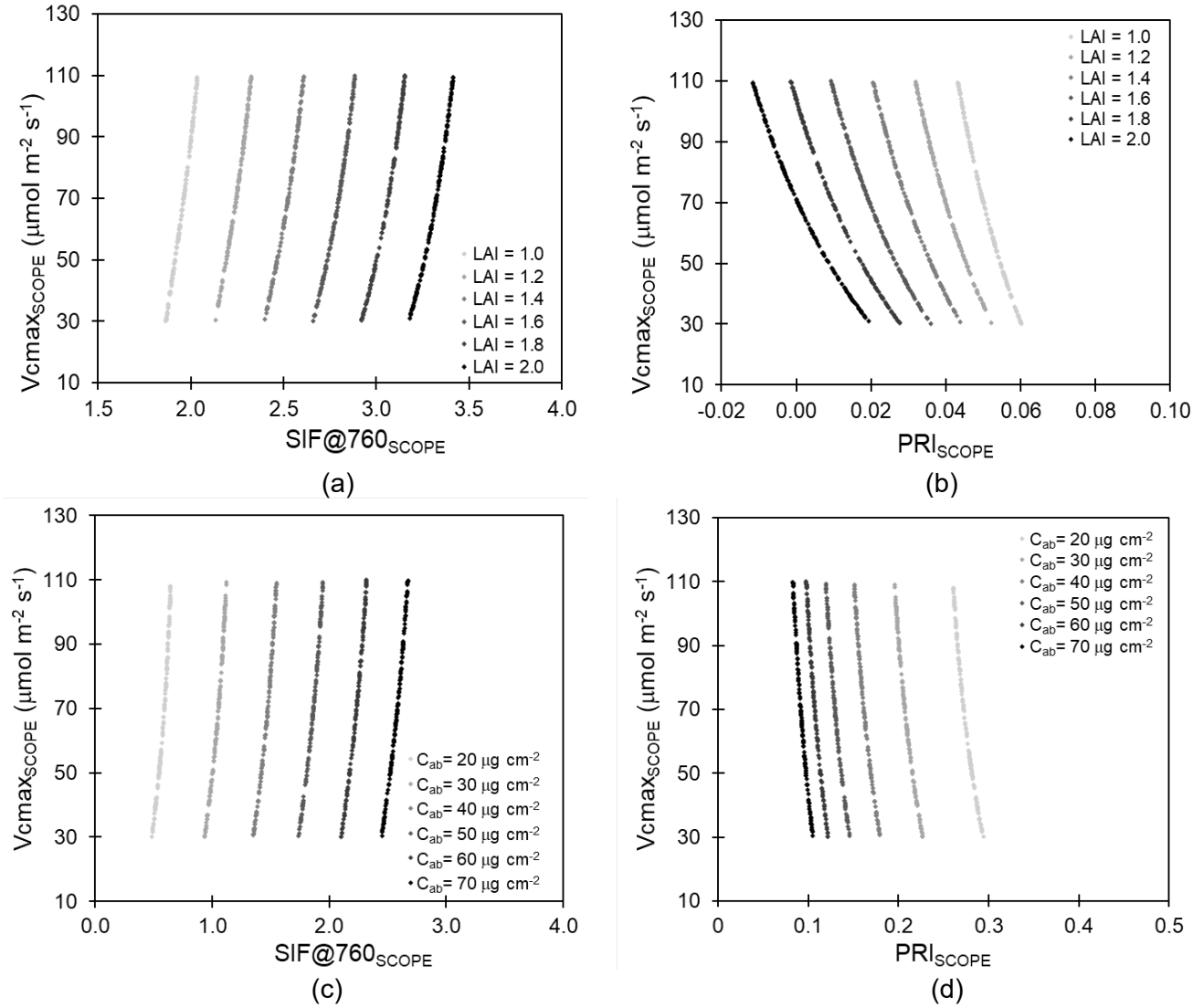

Figure 6. Results of modeling the effect of chlorophyll content and LAI variation on Vc_{max} vs sun-induced chlorophyll fluorescence calculated with the in-filling method at 760nm (a and c) and Vc_{max} vs PRI (b and d).

Vc_{max} derived from model inversion using the green spectral region presented more robust relationships vs. assimilation rates measured in the field for both days than those obtained from the reflectance indices described above (r^2=0.67-0.84, p-value<0.005). The relationships between Vc_{max} and assimilation showed a steady increasing trend until reaching a saturation around 100 µmol $m^{-2} \cdot s^{-1}$ (Figure 7). A comparison of the inverted and image spectrum for one monitored tree per treatment (Figure A2) and the retrieved parameter ranges per treatment (Figure A1) has been presented in the Appendix to this manuscript.

The results of applying the same model inversion method to other spectral regions did not yield as good results (Table 5).

Vc_{max} retrieved by model inversion showed higher maximum carboxylation rate for higher assimilation and overall better separability between treatments than commonly used vegetation indices (one-way ANOVA analysis p-value = 0.08; eta value $\eta = 0.5$ as opposed to $\eta = 0.1$-0.4) as it was estimated accounting for the structural differences across the experimental field (Figure 8b).

Table 5. Coefficients of determination (r^2) for the relationships between assimilation vs. the different vegetation indices and vs. Vc_{max} resulting from SCOPE model inversion using wavelet transforms over 4 different spectral regions.

Index	**r^2 (DOY: 218)**	**r^2 (DOY: 237)**	**r^2 (both days)**
Structural indices			
NDVI	0.38*	0.27*	0.25*
RDVI	0.38*	0.15	0.18*
EVI	0.39*	0.16	0.20*
MTVI	0.37*	0.16	0.13*
Chlorophyll indices			
CI	0.35*	0.13	0.27*
TCARI/OSAVI	0.15	0.04	0.11
SIPI	0.37*	0.05	0.23*
Indices based on the green region			
PRI	0.44*	0.32*	0.17*
PRI_{515}	0.41*	0.19	0.26*
PRI_{M1}	0.42*	0.18	0.26*
PRI_{M2}	0.47*	0.34*	0.24*
PRI_{M3}	0.41*	0.27*	0.21*
PRI_n	0.42*	0.33*	0.26*
Fluorescence indicators			
FLD	0.49*	0.64**	0.35*
Vc_{max} from SCOPE model inversion			
505 – 560 nm	0.67**	0.84***	0.56***
700 – 750 nm	0.41*	0.25	0.16*
505–650 nm & 700–750 nm	0.47*	0.09	0.12
500 – 750 nm	0.38*	0.05	0.21*

**p-value<0.1 **p-value<0.01 ***p-value<0.001*

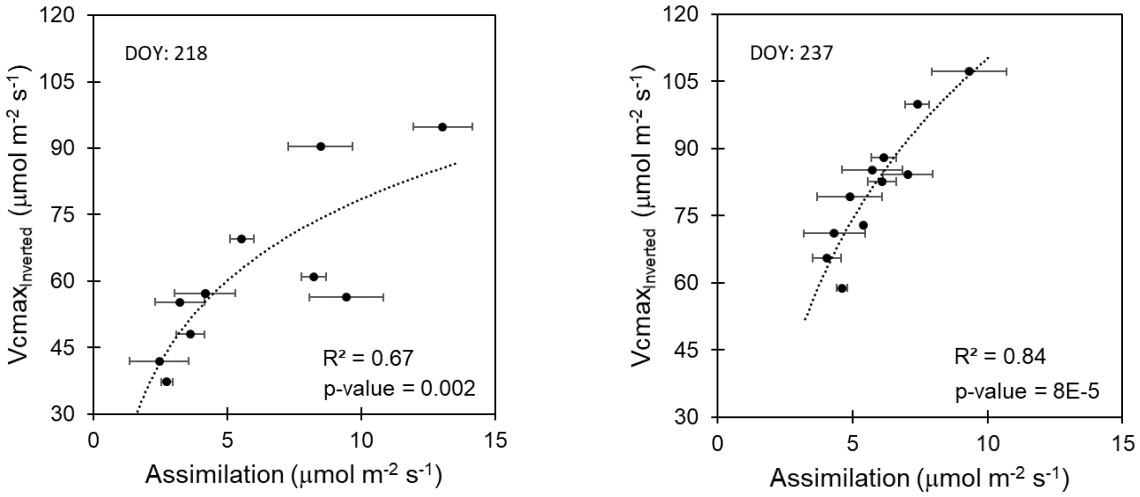

(a) (b)

Figure 7. Logarithmic relationships between Vc_{max} derived from SCOPE model inversion using the 505-560nm spectral region and assimilation rates measured in the field at both data acquisition dates DOY: 218 during kernel filling (a) and DOY: 237 after harvest (b). Error bars refer to standard deviation values for assimilation measurements in the field.

Both SIF and PRI followed the general trend of the differences found in assimilation rates. As expected, treatment blocks with higher assimilation rates (Figure 8a) also showed higher SIF in average (Figure 8c) and lower PRI (Figure 8d) corresponding to lower proportional content of photoprotective xanthophyll compounds. The means of both the Normalised Difference Vegetation Index (NDVI) and the Chlorophyll Index (CI) per treatment, indices developed to track vigour and chlorophyll changes, did not follow the trends of assimilation measured for each treatment as clearly as Vc_{max} (Figures 8e and 8f).

The analysis of Vc_{max} derived from model inversion using the green spectral region and A was shown to be more robust across dates, as displayed in Figure 9a and Table 5. On the other hand, SIF and PRI did not follow the same trend when both dates were analysed together, being highly affected by environmental conditions and illumination at the moment of the data capture. NDVI presented more stability over time although, as it is a proxy of tree vigour and only indirectly linked to assimilation rate, it did not show a strong relationship as Vc_{max} derived by model inversion.

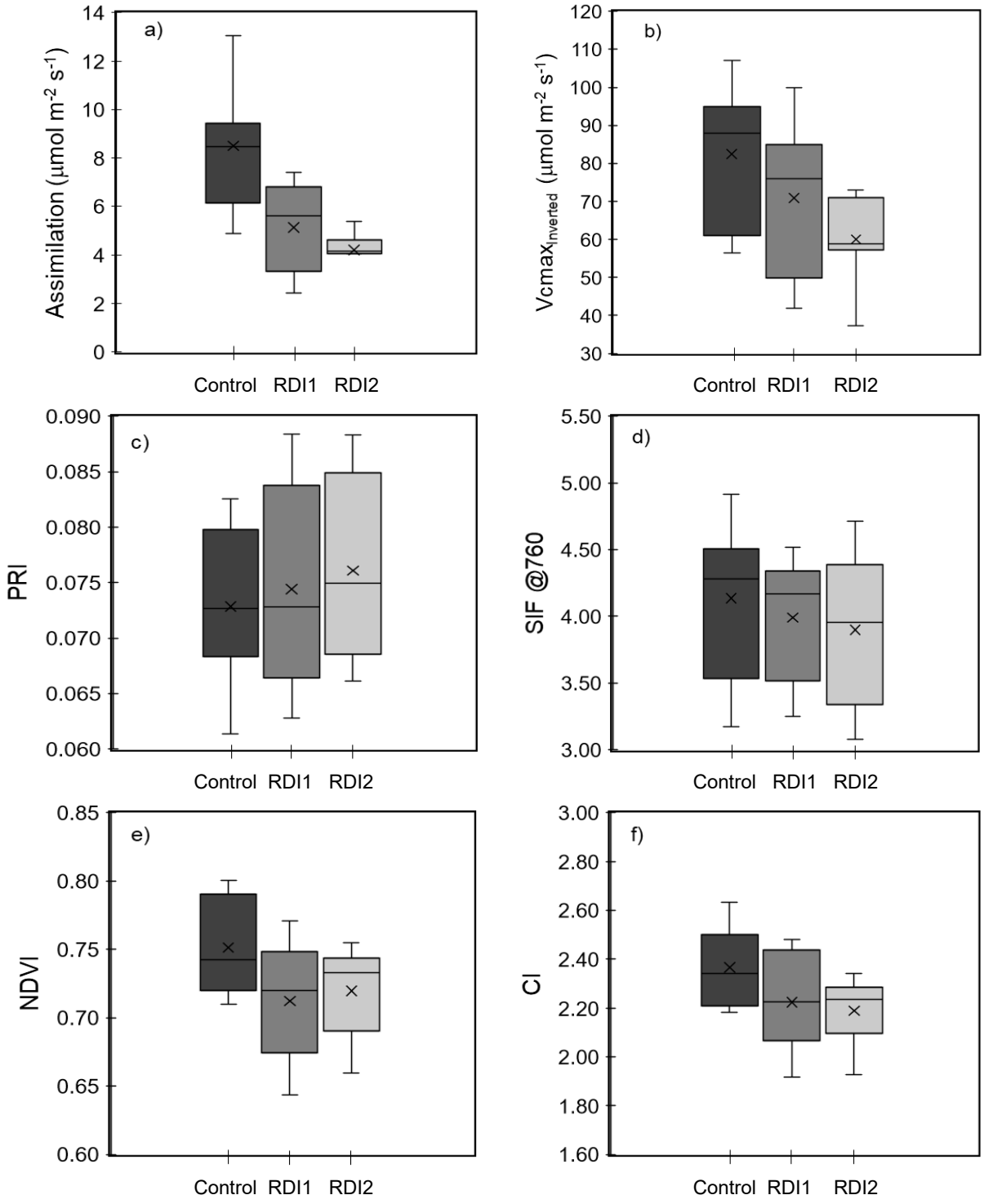

450

451 Figure 8. Ranges of variation found in crown averages for each treatment for assimilation rate (a),
452 Vc_{max} inverted using SCOPE (b), PRI derived from the hyperspectral image (c) and SIF calculated
453 from the image data using the in-filling method at 760 nm O_2-A band (d). Crossing line refers to
454 median value and box amplitude refers to the second and third quartiles' limits. Whiskers
455 represent the max and minimum data without outliers and middle 'x' refers to the mean value.

456

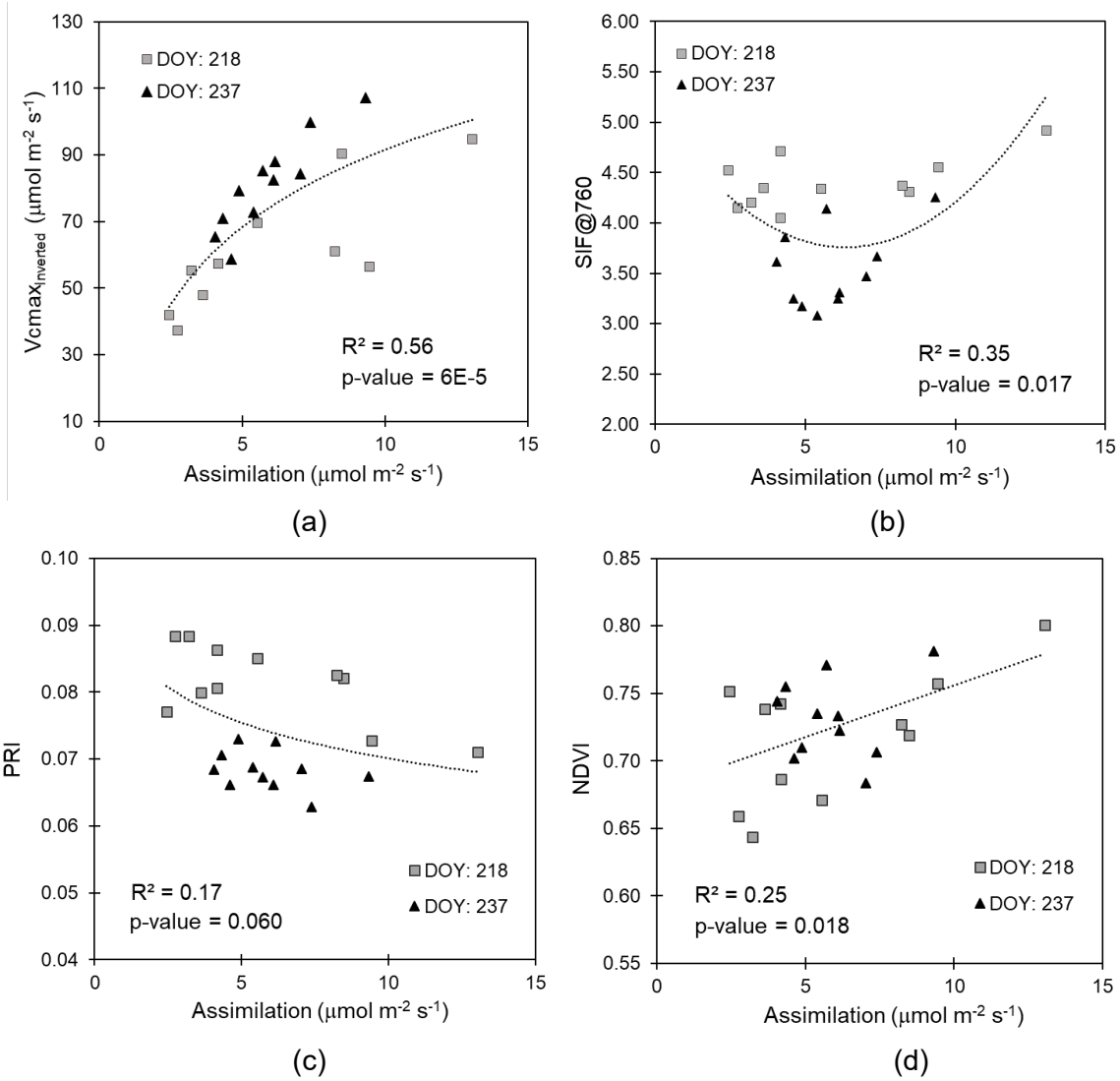

Figure 9. Relationships obtained between assimilation rate measured in the field and Vc_{max} derived from SCOPE model inversion using the green spectral region (a), SIF quantified from hyperspectral imagery through the FLD principle (b), PRI (c) and NDVI (d) spectral indices for all the measurements at kernel filling (DOY: 218) and at harvest (DOY: 237).

Discussion

According to the radiative transfer modelling analyses carried out to study the effects of Vc_{max} on the electromagnetic spectrum, the spectral regions that are affected by Vc_{max} changes are located in the green over the 505-560nm range and in the red-far red region between 650 and 800 nm, where chlorophyll fluorescence is emitted. This analysis is in agreement with the results obtained assessing different hyperspectral reflectance indices, which show stronger correlations between assimilation rates measured in the field and spectral indices based on green bands such as the Photochemical Reflectance Index (PRI) (Table 5) and SIF. It also suggests that those are the regions that need to be used to retrieve Vc_{max} through model inversion using SCOPE.

There is extensive literature that focuses on using the green and the chlorophyll fluorescence regions to detect pre-visual vegetation stress, that is, before changes are detectable by structural indices (Peñuelas *et al*., 1994; Thenot *et al*., 2002; Suarez *et al*., 2009; Flexas *et al*., 2000, 2002; Moya *et al*., 2004; Perez-Priego *et al*., 2005) and photosynthetic performance (Filella *et al*., 1996; Trotter *et al*., 2002; Evain *et al*., 2004). However, it has also been demonstrated that PRI indices are highly affected by illumination geometry, vegetation structure, pigment composition and soil background (Barton and North, 2001; Suarez *et al*., 2008), making their application over large areas challenging. Here we also show with physical modeling that the effects of LAI and chlorophyll content variations prevent PRI and SIF indices from having a direct universal link to assimilation rates (Figure 6). In addition to this, the methods using the PRI family of indices or SIF over time series require normalization techniques to account for the differences in illumination intensity at the time of image acquisition (Suarez *et al*., 2010, Zarco-Tejada *et al*., 2016) or within field structural or biophysical heterogeneity (Zarco-Tejada *et al*., 2013b; Koffi *et al*, 2015). Hence, these reasons suggest that methods based on spectral indices would fail at representing the variability of assimilation rate over time in crops where long-term stress has had an impact on growth and leaf composition.

In the past, new formulations and normalisations were developed to track plant traits overcoming confounding effects like LAI or pigment content (see PRI derived indices in Table 3; Haboudane *et al*., 2002; Zarco-Tejada *et al*., 2013; Woodgate *et al*., 2019). Still, these formulations end up being species specific and they need to be used in combination with empirical links to a particular trait. Established empirical relationships between vegetation indices and plant traits add another level of complexity as these relationships are highly empirical and difficultly transferable across fields and scales. The quantification of plant traits directly linked with plant functioning through physical model inversion allows vegetation monitoring precisely, being transferable and applicable over time series. In this study, we attempted the quantification of Vc_{max} to track the limitation in photosynthetic efficiency under stress. The method accounts for varying LAI and leaf chlorophyll content parameters to overcome the limitations pointed out in Figure 5 and the wide range of variation found in the field as a result of a long-term experimental design. We also assumed within-field variations in other pigments concentration, constituents and variations in leaf inclination distribution function which has demonstrated a very dynamic response to stress in almond trees (Egea *et al*., 2012). With SCOPE model we can simulate the effects of plant stress on the photosynthetic efficiency and the resulting reflectance signal under different illumination and ambient conditions (Van der Tol *et al*., 2014) ensuring the applicability of the method to time series of data.

One limitation of SCOPE model is that the canopy radiative transfer module assumes a continuum 1D layer, lacking the capacity of other models that account for full 3D structural parametrization of tree crowns. Previous work has proved that the quantification of Vc_{max} through SCOPE model inversion is achievable for wheat (Camino *et al*., 2019), a homogeneous single layer crop without woody elements and complex ramifications. Recent developments of SCOPE adapted the radiative transfer to account for the vertical heterogeneity of biophysical inputs across the canopy (Yang *et al*., 2017) but the capability of simulating tree crowns is still not present. Nevertheless, high resolution imagery allows extracting crown spectra from pure vegetation pixels. We applied

516 the model inversion to pure vegetation pixels and our results suggest that Vc_{max} derived from
517 model inversion can be used to track assimilation rates in orchard trees.

518 Inverting SCOPE to derive Vc_{max} using the green spectral region yielded better results with field-
519 measured assimilation rate (r^2= 0.7-0.8) than any other approach based on common narrow-band
520 spectral indices (r^2=0.3-0.5), SIF (r^2= 0.5-0.6) or model inversion using other spectral regions
521 (Table 5). Previous studies have inverted SCOPE to derive Vc_{max} based on the SIF signal, these
522 studies are either using satellite imagery with low spatial resolution (Zhang *et al*., 2014; 2018) or
523 are applied to continuous crops lacking the complex architecture of woody canopies (Camino *et*
524 *al*., 2019). Retrieving Vc_{max} for individual crowns using SCOPE poses extra challenges related to
525 the proper structural characterisation of the canopy with a model that does not account for
526 branching architecture and the presence of woody components. By employing the wavelet
527 transformed amplitude, the estimations are resulting from the local variation of reflectance
528 function of Vc_{max} response feature. This technique removes the effects of wider spectral region
529 variation while quantifying the narrow effects (Mittermayr *et al*., 2001) and has been suggested
530 as a method to minimise the effects of canopy structure on the spectral signal (Blackburn, 2006).
531 Hence the technique is not as affected by errors in atmospheric corrections as if the inversion is
532 based on the minimum spectral distance. This method has been used in the past to invert plant
533 traits from hyperspectral imagery yielding similar results (Blackburn and Ferwerda, 2008; Cheng
534 *et al*., 2011; Kattenborn *et al*., 2017). The use of the green region as opposed to the chlorophyll
535 fluorescence emission region has further benefits for future applicability of the method because
536 1) detectors have higher sensitivity over the visible part of the spectrum and the signal to noise
537 ratio is higher, 2) there are not narrow atmospheric absorption features, ensuring a more reliable
538 calibration regardless the quality of ancillary data measured in the field, 3) vegetation reflectance
539 in the green region typically varies within a 5% and does not present abrupt changes driven by
540 vegetation structure like in the red-far-red regions and 4) the absolute signal variation due to Vc_{max}
541 changes presents a higher proportional variation on the signal due to the higher absorption of

light in the visible. On the other hand, in the green region there is a high absorption due to different photosynthetic pigments, and it is a region where their temporal dynamics is not yet well understood, in particular under stress conditions.

The results suggest that the inverted maximum carboxylation rate increases linearly with assimilation measured in the field up to a saturation point. At that point, around 100 µmol m^{-2} s^{-1}, the maximum carboxylation rate is not limiting assimilation in a linear manner. Zarco-Tejada *et al*. (2016) found a similar trend between assimilation and SIF. This could be attributed to a non-linear relationship between assimilation and respiration as they are known to respond differently to environmental factors like temperature (Bowling *et al*., 2001; Knohl and Buchmann, 2005) and stress (Raggi, 1995; Reichstein *et al*., 2005). Further SCOPE model analysis shows how the air temperature has an effect on the relationship between Vc_{max} and assimilation (data not shown), this effect is still to be properly assessed in order to track assimilation rates for periods with highly changing environmental conditions. Another cause can be the potential variability of the J_{max}/Vc_{max} ratio, which has been demonstrated to vary with leaf temperature in almond trees (Egea *et al*., 2011).

The common trend followed by the results of both data acquisition days (p value<0.0001) indicates this method is applicable to time series without the need of further normalisation providing a reliable tool to quantitatively track photosynthetic rate in tree orchards using SCOPE. Although previous studies have successfully track Vc_{max} trends over time, these are limited to herbaceous crops over coarse spatial scales (Zhang *et al*., 2014). Previous methods also relied on the successful retrieval of SIF remotely, or require a high and accurate set of ancillary data (Guanter *et al*., 2014; Bayat *et al*., 2018). The results suggest the methodology presented in this study using the green spectral region properly accounts for existing biophysical variability and overcomes the confounding structural effects on the spectra while empirical models alone based on the same part of the spectrum could not fully track assimilation differences. Furthermore, this study demonstrates that an ultralight hyperspectral sensor can be flown on board unmanned

568 platforms (Thong *et al*., 2018; Lucieer *et al*., 2014), opening several avenues of future research
569 and applications in remote sensing science of plant functioning.

570

571 ## 4. Conclusions

572 The remote assessment of photosynthetic performance under stress is challenging due to the
573 confounding effects of varying structural and biophysical properties in woody crops such as in the
574 case of orchards. Here, we present a methodology that accounts for the variability in the structural
575 and pigment composition to quantify the maximum carboxylation rate (Vc_{max}) as an indicator of
576 photosynthetic rate reductions under stress through SCOPE model inversion. Results suggest
577 that the methodology presented overcomes the biophysical and illumination effects while narrow-
578 band spectral indices cannot fully assess assimilation differences across dates. The robustness
579 of the method has been demonstrated with datasets acquired at two different times along the
580 season. Finally, the lightweight specifications of the hyperspectral sensor used in this study allows
581 its use from both manned and unmanned platforms, providing a flexible, affordable and practical
582 means to both small and large area crop monitoring and assessment of plant functioning traits.

583

584 ## Acknowledgments

585 The experiment was carried out in the experimental farm “Alameda del Obispo” belonging to
586 IFAPA. The authors gratefully acknowledge the financial support of the Spanish Ministry of
587 Science and Education for projects AGL2012-40053-C03-01 and AGL2012-35196 and of the
588 Regional Government of Andalusia, Spain, for project P12-AGR-2521. Ignacio Lorite and Elías
589 Fereres are acknowledged for their support to this work. The authors would also like to thank R.
590 Romero, D. Notario, A. Vera, and A. Hornero for their technical support during the airborne
591 campaign and the image processing conducted in the QuantaLab-IAS-CSIC laboratory. M. López-

López, M. Orgaz, K. Gutiérrez, and R. Luque are also acknowledged for their fieldwork in the almond orchard.

References

Atzberger C. (2004) Object-based retrieval of biophysical canopy variables using artificial neural nets and radiative transfer models. *Remote Sensing of Environment*, 93(1-2), 53-67.

Atzberger C, Richter K. (2012) Spatially constrained inversion of radiative transfer models for improved LAI mapping from future Sentinel-2 imagery. *Remote Sensing of Environment*, 120, 208 −218.

Ball, J.T., Woodrow, I.E., Berry, J.A., 1987. In: Biggins, J. (Ed.), A Model Predicting Stomatal Conductance and its Contribution to the Control of Photosynthesis under Different Environmental Conditions BT - Progress in Photosynthesis Research: Volume 4 Proceedings of the VIIth International Congress on Photosynthesis Providence, Rhode Island, USA, August 10–15, 1986. Springer Netherlands, Dordrecht.

Barton, C. V. M., North, P. R. J. (2001). Remote sensing of canopy light use efficiency using the Photochemical Reflectance Index. Model and analysis. *Remote Sensing of Environment*, 78(264), 273.

Bayat, B., van der Tol, C., Verhoef, W. (2018). Integrating satellite optical and thermal infrared observations for improving daily ecosystem functioning estimations during a drought episode. *Remote Sensing of Environmen*t, 209, 375-394.

Blackburn, G.A. (2006). Hyperspectral remote sensing of plant pigments. *Journal of Experimental Botany*, 58(4), 855-867.

Blackburn, G.A., Ferwerda, J.G. 2008. Retrieval of chlorophyll concentration from leaf reflectance spectra using wavelet analysis. *Remote Sensing of Environment*, 112, 1614–1632.

Bowling, D.R., Tans, P.P., Monson, R.K. (2001), Partitioning net ecosystem carbon exchange with isotopic fluxes of CO2, *Global Change Biol*., 7(2), 127–145.

Broge, N.H., Leblanc, E. (2000). Comparing prediction power and stability of broadband and hyperspectral vegetation indices for estimation of green leaf area index and canopy chlorophyll density, *Remote Sensing of Environment*, 76, 156-172.

Camino C., González-Dugo V., Hernández P., and Zarco-Tejada. P. J., (2019) Radiative transfer Vcmax estimation from hyperspectral imagery and SIF retrievals to assess photosynthetic performance in rainfed and irrigated plant phenotyping trials, *Remote Sensing of Environment*, 231 (2019), p. 111186

Calderón, R., Navas-Cortés, J.A., Zarco-Tejada, P.J. (2015) Early Detection and Quantification of Verticillium Wilt in Olive Using Hyperspectral and Thermal Imagery over Large Areas, *Remote Sensing*, 7, 5584-5610; doi:10.3390/rs70505584.

Cescatti, A. (1997) Modelling the radiative transfer in discontinuous canopies of asymmetric crowns. I. Model structure and algorithms. *Ecological Modelling*, 101, 263-274.

Chaerle, L., Hagenbeek, D., Vanrobaeys, X., Van der Straeten, D. (2007). Easrly detection of nutrient and biotic stress in Phaseolus vulgaris. *International Journal of Remote Sensing*, 28(16), 3479-3492.

Cheng, T., Rivard, B. & Sanchez-Azofeifa, A. 2011. Spectroscopic determination of leaf water content using continuous wavelet analysis. *Remote Sensing of Environment,* 115, 659–670.

635 Collatz, G.J., Ball, J.T., Grivet, C., Berry, J.A. (1991) Physiological and environmental regulation
636 of stomatal conductance, photosynthesis and transpiration: A model that includes a laminar
637 boundary layer. *Agric. For. Meteorol*., 54, 107–136.

638 Combal, B., Baret, F., Poilvé, H., Polverin, U. (2001) Using multispectral reflectance to retrieve
639 LAI and chlorophyll content of maize and soybean. M. Leroy (Ed.), Physical measurements and
640 signatures in remote sensing, Aussois, France, 499-504.

641 Combal, B., Baret, F., Weiss, M., Trubuil, A., Macé, D., Pragnère, A., Myneni, R., Knyazikhin, Y.,
642 Wang, L. (2003) Retrieval of canopy biophysical variables from bidirectional reflectance: Using
643 prior information to solve the ill-posed inverse problem. *Remote Sensing of Environment*, 84(1),
644 1-15.

645 Courault, D., Seguin, B., Olioso, A. (2005) Review on estimation of evapotranspiration from
646 remote sensing data: From empirical to numerical modeling approaches. *Irrigation and Drainage*
647 *Systems*, 19, 223-249.

648 Cowan, I.R. (1978). In: Preston, R.D., Woolhouse, H.W.B.T.-A. (Eds.), Stomatal Behaviour and
649 Environment. Academic Press, pp. 117–228. https://doi.org/10.1016/S0065- 2296(08)60370-5.

650 Damm, A., Erler, A., Hillen, W., Meroni, M., Schaepman, M. E., Verhoef, W., & Rascher, U. (2011).
651 Modeling the impact of spectral sensor configurations on the FLD retrieval accuracy of sun-
652 induced chlorophyll fluorescence. *Remote Sensing of Environment*, 115, 1882–1892.

653 Damm, A., Guanter, L., Laurent, V.C.E., Schaepman, M.E., Schickling, A., Rascher, U. (2014)
654 FLD-based retrieval of sun-induced chlorophyll fluorescence from medium spectral resolution
655 airborne spectroscopy data. *Remote Sensing of Environment*, 147, 256-266.

656 Damm, A., Guanter, L., Paul-Limoges, E., van der Tol, C., Hueni, A., Buchmann, N., Eugster, W.,
657 Ammann, C., Schaepman, M. E. (2015a). Far-red sun-induced chlorophyll fluorescence shows
658 ecosystem-specific relationships to gross primary production: An assessment based on
659 observational and modeling approaches. *Remote Sensing of Environment*, 166, 91-105.

660 Damm, A., Guanter, L., Verhoef, W., Schaepfer, D., Garbari, S., Schaepman, M.E. (2015b) Impact
661 of varying irradiance on vegetation indices and chlorophyll fluorescence derived from
662 spectroscopy data. *Remote Sensing of Environment*, 156, 202-215.

663 Demmig, B., Winter, K., Krüger, A., Czygan, F.C. (1987) Photoinhibition and zeaxanthin formation
664 in intact leaves: a possible role of the xanthophyll cycle in the dissipation of excess light energy.
665 *Plant Physiology*, 84, 218–224.

666 Demmig-Adams, B. (1990). Carotenoids and photoprotection in plants: A role for the xanthophyll
667 zeaxanthin. Biochimica et Biophysica Acta (BBA) – *Bioenergetics*, 1020(1), 1-24.

668 Demmig-Adams, B., Adams, W.W. (1996) The role of xanthophyll cycle carotenoids in the
669 protection of photosynthesis. *Trends in Plant Science*, 1(1), 12-26.

670 Dungan, R.J., Turnbull, M.H., Kelly, D. (2007). The carbon costs for host trees of a phloem-feeding
671 herbivore. *Journal of Ecology*, 95, 603–613.

672 Egea, G., Gonzalez-Real, M.M., Baille, A., Nortes, P.A., Diaz-Espejo, A. (2011). Disentangling
673 the contributions of ontogeny and water stress to photosynthetic limitations in almond trees. *Plant,*
674 *Cell and Environment*, 34, 962-979.

675 Egea, G., Gonzalez-Real, M.M., Baille, A, Nortes, P.A., Conesa, M.R., Ruiz-Salleres, I. (2012).
676 Effects of water stress on irradiance acclimation of leaf traits in almond trees. *Tree Physiology*,
677 32, 450-463.

678 Espadafor, M., Orgaz, F., Testi, L., Lorite, I.J., Gonzalez-Dugo, V., Fereres, E. (2017). Responses
679 of transpiration and transpiration efficiency of almond trees to moderate stress deficits. *Scientia*
680 *Horticulturae*, 225, 6-14.

681 Evain, S., Flexas, J., Moya, I. (2004). A new instrument for passive remote sensing: 2.
682 Measurement of leaf and canopy reflectance changes at 531 nm and their relationship with
683 photosynthesis and chlorophyll fluorescence. *Remote Sensing of Environment*, 91, 175−185.

684 Farquhar, G.D., von Caemmerer, S., Berry, J.A. (1980), A biochemical-model of photosynthetic
685 CO2 assimilation in leaves of C-3 species, *Planta*, 149, 78–90.

686 Fereres, E., Goldhamer, D., Sadras, V. (2012) Yield Response to Water of Fruit Trees and Vines:
687 Guidelines. In: Steduto, P., Hsiao, T.C., Fereres, E., Raes, D. (Eds.), Crop Yield Response to
688 Water. Irrigation and Drainage Paper. Food and Agriculture Organization of the United Nations
689 (FAO). Rome, 246-296.

690 Filella, I., Amaro, T., Araus, J. L., Peñuelas, J. (1996). Relationship between photosynthetic
691 radiation use efficiency of barley canopies and the Photochemical Reflectance Index (PRI).
692 *Physiologia Plantarum*, 96, 211−216.

693 Flexas, J., Briantais, J. M., Cerovic, Z., Medrano, H., Moya, I. (2000). Steady-state and maximum
694 chlorophyll fluorescence responses to water stress in grapevine leaves: A new remote sensing
695 system. *Remote Sensing of Environment*, 73, 282−297.

696 Flexas, J., Escalona, J. M., Evain, S., Gulias, J., Moya, I., Osmond, C. B., *et al*. (2002). Steady-
697 state chlorophyll fluorescence (Fs) measurements as a tool to follow variations of net CO2
698 assimilation and stomatal conductance during water-stress in C-3 plants. *Physiologia Plantarum*,
699 114(2), 231−240.

700 Frankenberg, C., Fisher, J. B., Worden, J., Badgley, G., Saatchi, S. S., Lee, J. E., Toon, G. C.,
701 Butz, A., Jung, M., Kuze, A., and Yokota, T. (2011) New global observations of the terrestrial
702 carbon cycle from GOSAT: Patterns of plant fluorescence with gross primary productivity,
703 *Geophys. Res. Lett*., 38, https://doi.org/10.1029/2011GL048738.

704 Gamon, J., Penuelas, J.A., Field, C.B. (1992). A narrow-waveband spectral index that tracks
705 diurnal changes in photosynthetic efficiency. *Remote Sensing of Environment*, 41, 35-44.

706 Gamon, J. A., Filella, I., Peñuelas, J. (1993). The dynamic 531 nm reflectance signal: A survey of
707 twenty angiosperm species. In H. Y. Yamamoto, & C. M. Smith (Eds.), 1993, Photosynthetic
708 responses to the environment (pp. 172–177). Rockville, MD: American Society of Plant
709 Physiologists.

710 Gamon, J.A., Serrano, L., Surfus, J.S. (1997) The photochemical reflectance index: an optical
711 indicator of photosynthetic radiation use efficiency across species, functional types, and nutrient
712 levels. *Oecologia*, 112(4), 492-501.

713 Garrity, S.R., Eitel, J.U.H., Vierling, L.A. (2011). Disentangling the relationships between plant
714 pigments and the photochemical reflectance index reveals a new approach for remote estimation
715 of carotenoid content. *Remote Sensing of Environment*, 115 (2), 628-635.

716 Guanter, L., Zhang, Y., Jung, M., Joiner, J., Voigt, M., Berry, J. A., & Griffis, T. J. (2014). Global
717 and time-resolved monitoring of crop photosynthesis with chlorophyll fluorescence. *Proceedings*
718 *of the National Academy of Sciences (PNAS)*. http://dx.doi.org/10.1073/pnas.132000811.

719 Gueymard, C. (1995) SMARTS, a Simple Model of the Atmospheric Radiative Transfer of
720 Sunshine: Algorithms and Performance Assessment. Florida Solar Energy Center, Cocoa, FL
721 Technical report no. FSEC-PF-270–95.

722 Gueymard, C.A., Myers, D., Emery, K. (2002) Proposed reference irradiance spectra for solar
723 energy systems testing. *Solar Energy*, 73, 443–467. http://dx.doi.org/10.1016/ S0038-
724 092X(03)00005-7.

725 Haboudane, D., Miller, J. R., Tremblay, N., Zarco-Tejada, P. J., Dextraze, L. (2002). Integrated
726 narrow-band vegetation indices for prediction of crop chlorophyll content for application to
727 precision agriculture. *Remote Sensing of Environment*, 81, 416 – 426.

728 Haboudane, D., Miller, J.R., Pattey, E., Zarco-Tejada, P.J., Strachan, I.B. (2004). Hyperspectral
729 vegetation indices and novel algorithms for predicting green LAI of crop canopies: modeling and
730 validation in the context of precision agriculture. *Remote Sensing of Environment*, 90, 337-352.

731 Hernández-Clemente, R., Hornero, A., Mottus, M., Penuelas, J., González-Dugo, V., Jiménez,
732 J.C., Suárez, L., Alonso, L., & Zarco-Tejada, P.J. (2019) Early Diagnosis of Vegetation Health
733 From High-Resolution Hyperspectral and Thermal Imagery: Lessons Learned From Empirical
734 Relationships and Radiative Transfer Modelling, *Current Forestry Reports*, 5, 169–183,
735 https://doi.org/10.1007/s40725-019-00096-1.

736 Hsiao T.C., Fereres E., Acevedo E., Henderson D.W. (1976) Water Stress and Dynamics of
737 Growth and Yield of Crop Plants. In: Lange O.L., Kappen L., Schulze ED. (eds) Water and Plant
738 Life. Ecological Studies (Analysis and Synthesis), vol 19. Springer, Berlin, Heidelberg.

739 Hsiao, T.C., Bradford, K.J. (1983) Physiological Consequences of Cellular Water Deficits1sa. In:
740 H. M. Taylor, J. R. Wayne, S. R. Thomas, editors, Limitations to Efficient Water Use in Crop
741 Production, ASA, CSSA, SSSA, Madison, WI. p. 227-265.
742 doi:10.2134/1983.limitationstoefficientwateruse.c15.

743 Huete, A., Didan, K., Miura, T., Rodriguez, E. P., Gao, X., Ferreira, L. G. (2002). Overview of the
744 radiometric and biophysical performance of the MODIS vegetation indices. *Remote Sensing of*
745 *Environment*, 83, 195-213.

746 Ihuoma, S.O., Madramootoo, C.A. (2017) Recent advances in crop water stress detection.
747 *Computer and Eletronics in Agriculture*, 141, 267-275.

748 Jacquemoud, S., Verhoef, W., Baret, W., Bacour, C., Zarco-Tejada, P.J., Asner, G.P., François,
749 C., Ustin, S.L. (2009) PROSPECT+SAIL models: A review of use for vegetation characterization,
750 *Remote Sensing of Environment*, 113, S56-S66.

751 Kattenborn, T., Fassnacht, F.E., Pierce, S., Lopatin, J., Grim, J.P., Schmidtlein, S. (2017) Linking
752 plant strategies and plant traits derived by radiative transfer modelling. *Journal of Vegetation*
753 *Science*, 28, 717-727.

754 Kimball, B.A. (1983) Carbon dioxide and agricultural yield: an assemblage and analysis of 430
755 prior observations. *Agron. J.*, 75, 779-788.

Knohl, A., Buchmann, N. (2005). Partitioning the net CO2 flux of a deciduous forest into respiration and assimilation using stable carbon isotopes. *Global Biogeochemical Cycles*, 19(4). doi:10.1029/2004GB002301.

Koffi, E.N., Rayner, P.J., Norton, A.J., Frankenberg, C., Scholze, M. (2015) Investigating the usefulness of satellite-derived fluorescence data in inferring gross primary productivity within the carbon cycle data assimilation system. *Biogeosciences*, 12, 4067–4084.

Krause, G.H., Weis, E. (1991) Chlorophyll fluorescence and photosynthesis: The basics. *Annu. Rev. Plant Physiol. Plant Mol. Biol*., 42, 313-349.

Laurent, V.C.E., Schaepment, M.E., Verhoef, W., Weyermann, J., Chavez, R.O. (2014) Bayesian object-based estimation of LAI and chlorophyll from a simulated Sentinel-2 top-of-atmosphere radiance image. *Remote Sensing of Environment*, 140, 318-329.

Law, B.E., Cescatti, A., Baldocchi, D.D. (2001) Leaf area distribution and radiative transfer in open-canopy forests: implications for mass and energy exchange. *Tree physiology*, 21(12-13), 777-787.

Lichtenthaler, H.K., Wenzel, O., Buschmann, C., Gitelson, A. (1998) Plant stress detection by reflectance and fluorescence. *Annals of the New York Academy of Sciences*, 851, 271-285.

Lobell, D.B., Cassman, K.G., Field, C.B. (2009) Crop Yield Gaps: Their importance, Magnitudes, and Causes. *Annual Review of Environment and Resources*, 34, 179-204.

Long, S.P., Marshall-Colon, A., Zhu, X.G. (2015) Meeting the global food demand of the future by engineering crop photosynthesis and yield potential. *Cell*, 161(1), 56-66.

Lopez-Lopez, M., Espadafor, M., Testi, L., Lorite, I.J., Orgaz, F., Fereres, E. (2018). Water use efficiency of irrigated almond trees when subjected to water deficits. *Agricultural Water Management*, 195, 84-93.

Lucieer, A., Malenovsky, Z., Veness, T., Wallace, L. (2014). HyperUAS - Imaging spectroscopy from a multirotor unmanned aircraft system. *Journal of Field Robotics*, 31 (4), 571-590.

Meroni, M., Rossini, M., Guanter, L., Alonso, L., Rascher, U., Colombo, R. (2009). Remote sensing of solar-induced chlorophyll fluorescence: Review of methods and applications. *Remote Sensing of Environment*, 113, 2037–2051.

Mittermayr, C.R., Tan, H.W., Brown, S.D. (2001). Robust calibration with respect to background variation. *Applied Spectroscopy*, 55, 827-833.

Mohammed, G.H., W.D. Binder and S.L. Gillies. 1995. Chlorophyll fluorescence: A review of its practical forestry applications and instrumentation. *Scand. J. For. Res*., 10, 383-410.

Mohammed, G.H., Colombo, R., Middleton, E.M., Rascher, U., van der Tol, C., Nedbal, L., Goulas, Y., Pérez-Priego, O., Damm, A., Meroni, M., Joiner, J., Cogliati, S., Verhoef, W., Malenovský, Z., Gastellu-Etchegorry, J.P., Miller, J.R., Guanter, L., Moreno, J., Moya, I., Berry, J.A., Frankenberg, C., Zarco-Tejada, P.J. (2019) Remote sensing of solar-induced chlorophyll fluorescence (SIF) in vegetation: 50 years of progress, *Remote Sensing of Environment*, 231, 111177. https://doi.org/10.1016/j.rse.2019.04.030.

Moya, I., Camenen, L., Evain, S., Goulas, Y., Cerovic, Z.G., Latouche, G., Flexas, J., Ounis, A. (2004) A new instrument for passive remote sensing: 1. Measurements of sunlight-induced chlorophyll fluorescence. *Remote Sens. Environ*., 91, 186–197.

Nichol, C. J., Lloyd, J., Shibistova, O., Arneth, A., Röser, C., Knohl, A., Matsubara, S., Grace, J. (2002). Remote sensing of photosynthetic-light-use-efficiency of a Siberian boreal forest. *Tellus*, 54B, 677−687.

Papageorgiou, G. (1975). Chlorophyll fluorescence: An intrinsic probe of photosynthesis. In Govindjee (Ed.), Bioenergetics of photosynthesis (pp. 319−371). New York: Academic Press.

Pérez-Priego, O.; Zarco-Tejada, P.J.; Miller, J.R.; Sepulcre-Cantó, G.; Fereres, E. (2005) Detection of water stress in orchard trees with a high-resolution spectrometer through chlorophyll fluorescence In-Filling of the O2-A band. *IEEE Trans. Geosci. Remote Sens*., 43, 2860–2868.

Peñuelas, J., Gamon, J.A., Fredeen, A.L., Merino, J., Field, C.B. (1994). Reflectance Indices Associated with Physiological Changes in Nitrogen- and Water-Limited Sunflower leaves. *Remote Sensing of Environment*, 48, 135-146.

Plascyk, J.A., Gabriel, F.C. (1975). The Fraunhofer line discriminator MKII an airborne instrument for precise and standardized ecological luminescence measurement. *IEEE Trans. Instrum. Meas*., 24, 306–313.

Peñuelas J., Filella, I., Baret, F. (1995). Semiempirical indices to assess carotenoids/chlorophyll a ratio from leaf spectral reflectance. *Photosynthetica*, 31, 221-230.

Raggi, V. (1995). CO2 assimilation, respiration and chlorophyll fluorescence in peach leaves infected by Taphrina deformans, *Physiol. Plant*. 93: 540-544.

Rascher, U., Agati, G., Alonso, L., Cecchi, G., Champagne, S., Colombo, R., *et al*. (2009). CEFLES2: The remote sensing component to quantify photosynthetic efficiency from the leaf to the region by measuring sun-induced fluorescence in the oxygen absorption bands. *Biogeosciences Discussions*, 6(7), 2217–2266.

Reichstein, M., Falge, E., Baldocchi, D., Papale, D., Aubinet, M., Berbigier, P., Bernhofer, C., Buchmann, N., *et al*. (2005) On the separation of net ecosystem exchange into assimilation and ecosystem respiration: review and improved algorithm. *Glob. Chang. Biol*., 11, 1424-1439.

Richardson, A. D., Berlyn, G. P. (2002). Spectral reflectance and photosynthetic properties of Betula papyrifera (Betulaceae) leaves along an elevational gradient on Mt. Mansfield, Vermont, USA. *American Journal of Botany*, 89(1), 88−94.

Richardson, A. D., Berlyn, G. P., & Duigan, S. P. (2003). Reflectance of Alaskan black spruce foliage in relation to elevation and latitude. *Tree Physiology*, 23, 537−544.

Rosema, A., Verhoef, W., Noorbergen, H., Borgesius, J. J. (1992). A new forest light interaction model in support of forest monitoring, *Remote Sens. Environ*., 42(1), 23–41.

Rougean, J.L., Breon, F.M. (1995). Estimating PAR absorbed by vegetation from bidirectional reflectance measurements. *Remote Sensing of Environment*, 51, 375-384

Rouse, J.W., Hass, R.H., Schell, J.A., Deering, D.W., 1973. Monitoring vegetation systems 742 in the great plains with ERTS. Third Earth Resour. Technol. Satell. Symp. 1, 309–317. 743 https://doi.org/citeulike-article-id:12009708

834 Running, S.W., Baldocchi, D.D., Turner, D.P., Gower, S.T., Bakwin, P.S., Hibbard, K.A. (1999) A
835 global Terrestrial Monitoring Network Integrating Tower Fluxes, Flask Sampling, Ecosystem
836 Modeling and EOS Satellite Data. *Remote Sensing of Environment*, 70(1), 108-127.

837 Savitzky, A., Golay, M.J.E. (1964). Smoothing and Differentiation of Data by Simplified Least
838 Squares Procedures. *Analytical Chemistry*, 36 (8), 1627–39. doi:10.1021/ac60214a047.

839 Schurr, U., Walter, A., Rascher, U. (2006). Functional dynamics of plant growth and
840 photosynthesis – from steady-state to dynamics – from homogeneity to heterogeneity. *Plant, Cell*
841 *and Environment*, 29, 340-352.

842 Serbin, S.P., Dillaway, D.N., Kruger, E.L., & Townsend, P.A. (2012). Leaf optical properties reflect
843 variation in photosynthetic metabolism and its sensitivity to temperature. *Journal of Experimental*
844 *Botany*, 63, 489–502, http://dx.doi.org/10.1093/jxb/err294.

845 Serbin, S.P., Singh, A., Desai, A.R., Dubois, S.G., Jablonski, A.D, Kingdon, C.C., Kruger, E.L.,
846 Townsend, P.A. (2015). Remotely estimating photosynthetic capacity, and its response to
847 temperature, in vegetation canopies using imaging spectroscopy. *Remote Sensing of*
848 *Environment*, 167, 78-87.

849 Stagakis, S., González-Dugo, V., Cid, P., Guillén-Climent, M.L., Zarco-Tejada, P.J. (2012)
850 Monitoring water stress and fruit quality in an orange orchard under regulated deficit irrigation
851 using narrow-band structural and physiological remote sensing indices, *ISPRS Journal of*
852 *Photogrammetry and Remote Sensing*, 71, 47-61.

853 Stylinski, C.D., Oechel, W.C., Gamon, J.A., Tissue, D.T., Miglietta, F., Raschi, A. (2000) Effects
854 of lifelong [CO2] enrichment on carboxylation and light utilization of Quercus pubescens Willd.
855 examined with gas exchange, biochemistry and optical techniques. *Plant, Cell and Environment*,
856 23, 1353–1362.

857 Suárez, L., Zarco-Tejada, P.J., Sepulcre-Cantó, G., Pérez-Priego, O., Miller, J.R., Jiménez-
858 Muñoz, J.C., Sobrino, J. (2008) Assessing Canopy PRI for Water Stress detection with Diurnal
859 Airborne Imagery, *Remote Sensing of Environment*, 112, 560-575.

860 Suárez, L., Zarco-Tejada, P.J., Berni, J.A.J., González-Dugo, V., Fereres, E. (2009) Modelling
861 PRI for Water Stress Detection using Radiative Transfer Models., *Remote Sensing of*
862 *Environment*, 113, 730-744.

863 Suárez, L., Zarco-Tejada, P.J., González-Dugo, V., Berni, J.A.J., Sagardoy, R., Morales, F.,
864 Fereres, E. (2010) Detecting water stress effects on fruit quality in orchards with time-series PRI
865 airborne imagery, *Remote Sensing of Environment*, 114, 286-298.

866 Thenot, F., Méthy, M., & Winkel, T. (2002). The Photochemical Reflectance Index (PRI) as a
867 water-stress index. *International Journal of Remote Sensing*, 23(23), 5135−5139.

868 Tremblay, N., Wang, Z., Cerovic, Z.G. (2011). Sensing crop nitrogen status with fluorescence
869 indicators. A review. *Agronomy for sustainable Development*, 32, 451-464.

870 Trotter, G. M., Whitehead, D., & Pinkney, E. J. (2002). The Photochemical Reflectance Index as
871 a measure of photosynthetic light use efficiency for plants with varying foliar nitrogen contents.
872 *International Journal of Remote Sensing*, 23(6), 1207−1212.

873 Van der Tol, C., Verhoef, W., Timmermans, J., Verhoef, A., Su, Z. (2009) An integrated model of
874 soil-canopy spectral radiances, photosynthesis, fluorescence, temperature and energy balance.
875 *Biogeosciences*, 6(12), 3109–3129.

876 Van der Tol, C., Berry, J.A., Campbell, P.K.E., Rascher, U. (2014) Models of fluorescence and
877 photosynthesis for interpreting measurements of solar-induced chlorophyll fluorescence. *J.*
878 *Geophys. Res. Biogeosciences*, 119(12), 2312–2327.

879 Verhoef, W. (1984) Light Scattering by Leaf layers with Application to Canopy Reflectance
880 Modeling: the SAIL Model. *Remote Sensing of Environment*, 16, 125-141.

881 Verhoef, W. (2005). Extension of SAIL to model solar-induced canopy fluorescence spectra. 2nd
882 International Workshop on Remote Sensing of Vegetation Fluorescence, 17–19 Nov. 2004,
883 Montreal, Canada.

884 Verma, M., Schimel, D., Evans, B., Frankenberg, C., Beringer, J., Drewry, D.T., Magney, T.,
885 Marang, I., Hutley, L., Moore, C., Eldering, A. (2017), Effect of environmental conditions on the
886 relationship between solar-induced fluorescence and gross primary productivity at an OzFlux
887 grassland site, *J. Geophys. Res. Biogeosci*., 122, 716–733, doi:10.1002/2016JG003580.

888 Verrelst, J., Schaepman, M.E., Malenovský, Z., Clevers, J.G.P.W. (2010). Effects of woody
889 elements on simulated canopy reflectance: Implications for forest chlorophyll content retrieval.
890 *Remote Sensing of Environment*, 114(3), 647-656.

891 Verstraete, M.M., Pinty, B., Dickinson, R.E. (1990) A physical model of the bidirectional
892 reflectance of vegetation canopies. 1. Theory. *Journal of Geophysical Research*, 95, 11765-
893 11775.

894 Vilfan, N., van der Tol, C., Muller, O., Rascher, U., Verhoef, W. (2016) Fluspect-B: A model for
895 leaf fluorescence, reflectance and transmittance spectra. *Remote Sens. Environ*., 186:596–615.

896 Whitehead, D., Boelman, N. T., Turnbull, M. H., Griffin, K. L., Tissue, D. T., Barbour, M. M., *et al*.
897 (2005). Photosynthesis and reflectance indices for rainforest species in ecosystems undergoing
898 progression along a soil fertility chronosequence in New Zealand. *Oecologia*, 144, 233−244.

899 Widlowski, J-L., Pinty, B., Lavergne, T., Verstraete, M.M., Gobron, N. (2006) Horizontal radiation
900 transport in 3-D forest canopies at multiple spatial resolutions: Simulated impact on canopy
901 absorption. *Remote Sensing of Environment*, 103, 379-397.

902 Woodgate, W., Suarez, L., van Gorsel, E., Cernusak, L., Devilla, R., Held, A., Hughes, D., Norton,
903 A. (2019) tri-PRI: A three band reflectance index tracking dynamic photoprotective mechanisms
904 in a mature eucalypt forest. *Agriculture and Forest Meteorology*, 272-273, 187-201.

905 Woodward, F.I., Smith, T.M., Emanuel, W.R. (1995) A global land primary productivity and
906 phytogeography model. *Global Biogeochem. Cycles*, 9, 471–490.

907 Xu, L., & Baldocchi, D.D. (2003). Seasonal trends in photosynthetic parameters and stomatal
908 conductance of blue oak (Quercus douglasii) under prolonged summer drought and high
909 temperature. *Tree Physiology*, 23, 865–877.

910 Yang, P., Verhoef, W., van der Tol, C. (2017) The mSCOPE model: A simple adaptation to the
911 SCOPE model to describe reflectance, fluorescence and photosynthesis of vertically
912 heterogeneous canopies. *Remote Sens. Environ*., 201:1–11.

Zarco-Tejada, P.J., Miller, J.R., Mohammed, G.H., Noland, T.L., Sampson, P.H. (2001) Scaling-up and Model Inversion methods with narrow-band Optical Indices for Chlorophyll Content Estimation in closed Forest Canopies with Hyperspectral Data, *IEEE Transactions on Geoscience and Remote Sensing*, 39(7), 1491-1507.

Zarco-Tejada, P.J., Berni, J.A.J., Suárez, L., Sepulcre-Cantó, G., Morales, F., Miller, J.R. (2009) Imaging Chlorophyll Fluorescence from an Airborne Narrow-Band Multispectral Camera for Vegetation Stress Detection, *Remote Sensing of Environment*, 113, 1262-1275.

Zarco-Tejada, P.J., González-Dugo, V., Berni, J.A.J. (2012) Fluorescence, temperature and narrow-band indices acquired from a UAV platform for water stress detection using a micro-hyperspectral imager and a thermal camera, *Remote Sensing of Environment*, 117, 322-337.

Zarco-Tejada, P.J., Suárez, L., González-Dugo, V. (2013a) Spatial resolution effects on chlorophyll fluorescence retrievals in a heterogeneous canopy using hyperspectral imagery and radiative transfer simulation, *Geoscience and Remote Sensing Letters*, DOI:10.1109/LGRS.2013.2252877.

Zarco-Tejada, P.J., González-Dugo, V., Williams, L.E., Suárez, L., Berni, J.A.J., Goldhamer, D., Fereres, E. (2013b) A PRI-based water stress index combining structural and chlorophyll effects: assessment using diurnal narrow-band airborne imagery and the CWSI thermal index, *Remote Sensing of Environment*, 138, 38-50.

Zarco-Tejada, P.J., González-Dugo, M.V., Fereres, F. (2016). Seasonal stability of chlorophyll fluorescence quantified from airborne hyperspectral imagery as an indicator of net photosynthesis in the context of precision agriculture, *Remote Sensing of Environment*, 179, 15, 89–103.

Zarco-Tejada, P.J., Camino, C., Beck, P.S.A., Calderon, R., Hornero, A., Hernández-Clemente, R., Kattenborn, T., Montes-Borrego, M., Susca, L., Morelli, M., Gonzalez-Dugo, V., North, P.R.J., Landa, B.B., Boscia, D., Saponari, M., Navas-Cortes, J.A. (2018) Pre-visual symptoms of Xylella fastidiosa infection revealed in spectral plant-trait alterations, *Nature Plants*, DOI: 10.1038/s41477-018-0189-7.

Zhang, Y., Guanter, L., Berry, J.A., Joiner, J., van der Tol, C., Huete, A., Gitelson, A., Voigt, M., Köhler, P., 2014. Estimation of vegetation photosynthetic capacity from space-based measurements of chlorophyll fluorescence for terrestrial biosphere models. *Global Change Biology*, 20, 3727–3742.

Zhang, Y., Guanter, L., Joiner, J., Song, L., Guan, K., 2018. Spatially-explicit monitoring of crop photosynthetic capacity through the use of space-based chlorophyll fluorescence data. *Remote Sensing of Environment*, 210, 362–374.

Zhong, Y., Wang, X., Xu, Y., Wang, S., Jia, T., Hu, X., Zhao, J., Wei, L., Zhang, L. (2018) Mini-UAV-Borne Hyperspectral Remote Sensing: From Observation and Processing to Applications, *IEEE Geoscience and Remote Sensing*, 6(4), 46-62.

List of figure captions:

Figure 1. Overview of the image captured over the experimental field on DOY 160 (a) with the control blocks in green (C), RD1 blocks in yellow and RD2 blocks in red. Zoom of the automatic segmentation applied to one tree of each treatment (b), example reflectance and radiance spectrum from a tree of the control group (c).

Figure 2. Average radiance and reflectance spectrum for each of the treatments over the 400-800nm spectral range (a and d), zooms over the green (500-560 nm) region (b and e) and far-red-NIR (700-800 nm) region (c and f) where physical models indicate Vcmax change effects.

Figure 3. Results of simulating the spectral response to Vcmax variation over the range 10 to 250 μmol m^{-2} s^{-1} leaving the rest of parameters fixed (LAI=3, Cab=80, Cm=Cw=0.02) for the full 400-800nm range (a), for the 650-800nm region (b) and for 505-565 nm region (c). Reflectance difference between the maximum and minimum feature result of Vcmax variation is represented in a dotted line. (d) reflectance difference represented for 200 simulations with Vcmax ranging from 0 to 250 μmol m^{-2} s^{-1} over the green spectral feature.

Figure 4. Overview of the methodology used to retrieve Vcmax through SCOPE model inversion including hyperspectral image calibration, SCOPE parametrisation and input preparation and SCOPE model inversion.

Figure 5. Ranges of variation for the four physiological variables measured in the field at both dates: Assimilation rate (a), stomata conductance (b), steady-state fluorescence (c) and SPAD chlorophyll index (d). Crossing line refers to median value and box amplitude refers to the second and third quartiles' limits. Whiskers represent the max and minimum data without outliers.

Figure 6. Results of modeling the effect of chlorophyll content and LAI variation on Vcmax vs sun-induced chlorophyll fluorescence calculated with the in-filling method at 760nm (a and c) and Vcmax vs PRI (b and d).

Figure 7. Logarithmic relationships between Vcmax derived from SCOPE model inversion using the 505-560nm spectral region and assimilation rates measured in the field at both data acquisition dates DOY: 218 during kernel filling (a) and DOY: 237 after harvest (b). Error bars refer to standard deviation values for assimilation measurements in the field.

Figure 8. Ranges of variation found in crown averages for each treatment for assimilation rate (a), Vcmax inverted using SCOPE (b), PRI derived from the hyperspectral image (c) and SIF calculated from the image data using the in-filling method at 760 nm O_2-A band (d). Crossing line refers to median value and box amplitude refers to the second and third quartiles' limits. Whiskers represent the max and minimum data without outliers and middle 'x' refers to the mean value.

Figure 9. Relationships obtained between assimilation rate measured in the field and Vcmax derived from SCOPE model inversion using the green spectral region (a), SIF quantified from hyperspectral imagery through the FLD principle (b), PRI (c) and NDVI (d) spectral indices for all the measurements at kernel filling (DOY: 218) and at harvest (DOY: 237).

Figure A1. Results of modeling the relationship between Vcmax and assimilation rate for a standard set of inputs, the atmospheric conditions used for one of the days in this study and a air temperature ranging from 29 to 36 degrees.

Figure A2. Ranges of variation of SCOPE input parameter inversion for each treatment for chlorophyll (a), carotenoid (b), anthocyanin (c), LAI (d), water (e) and dry matter content (f). Crossing line refers to median value and box amplitude refers to the second and third quartiles'

994 limits. Whiskers represent the max and minimum data without outliers and middle ‘x’ refers to the
995 mean value.

996 Figure A3. Comparison of spectra obtained from SCOPE model inversion and image average
997 spectra for one monitored tree per treatment: Control (a), RDI1 (b) and RDI2 (c).

998

Appendix. SCOPE model inversion results

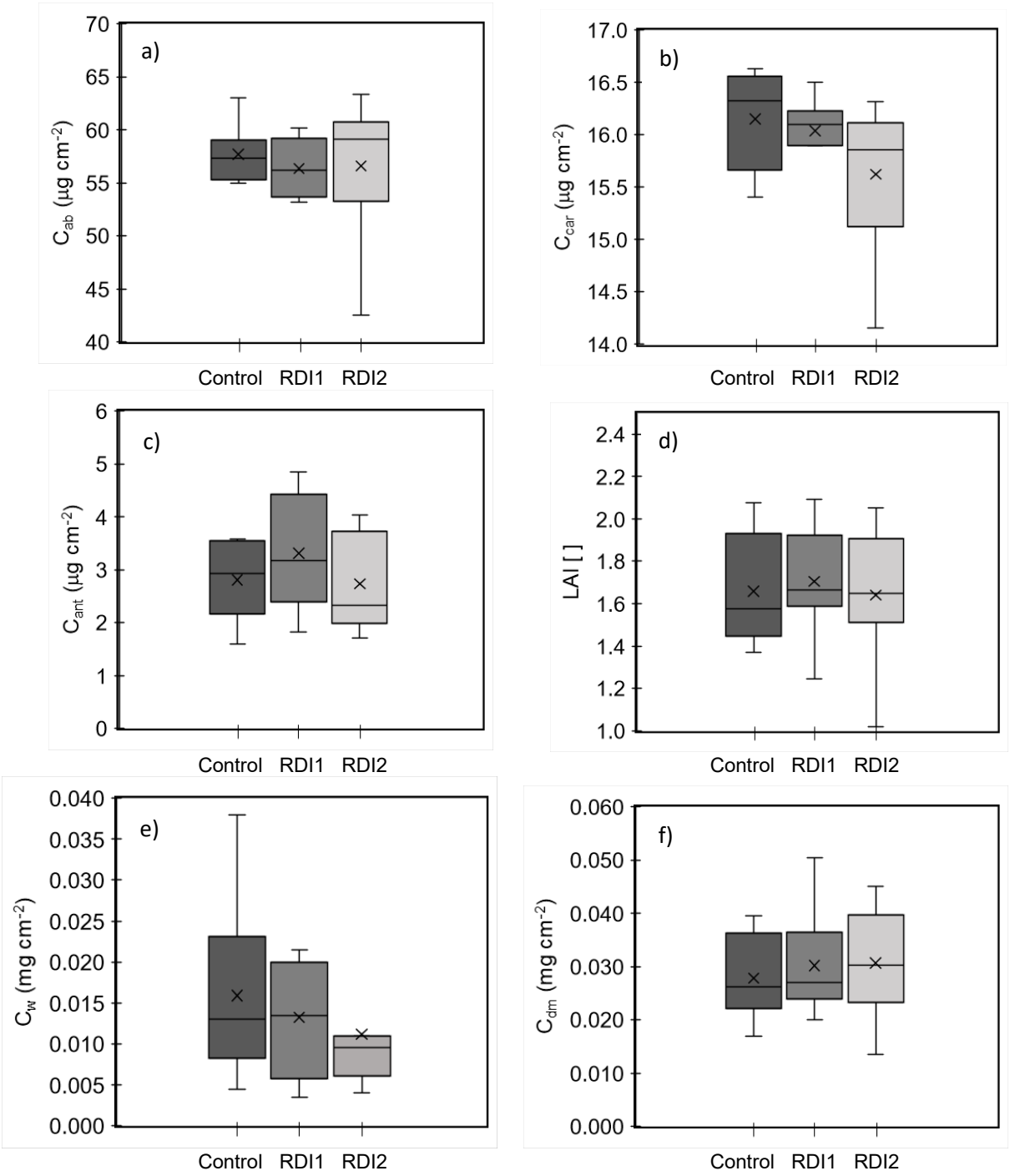

Figure A1. Ranges of variation of SCOPE input parameter inversion for each treatment for chlorophyll (a), carotenoid (b), anthocyanin (c), LAI (d), water (e) and dry matter content (f). Crossing line refers to median value and box amplitude refers to the second and third quartiles' limits. Whiskers represent the max and minimum data without outliers and middle 'x' refers to the mean value.

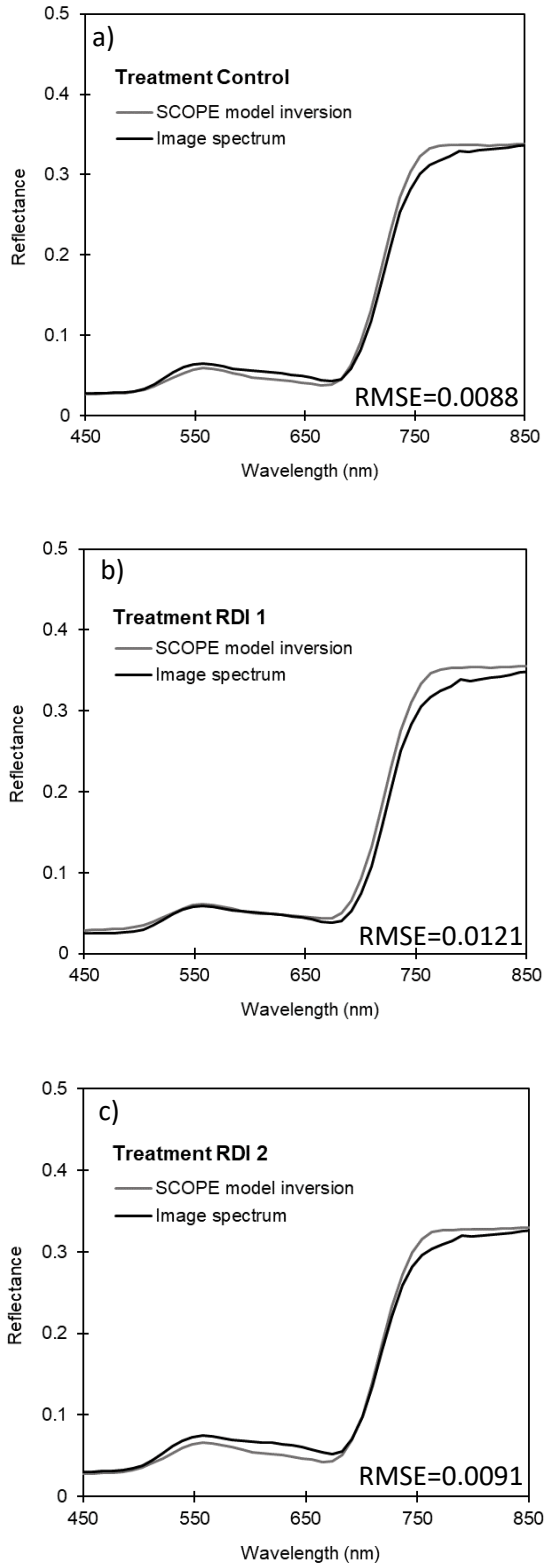

1007

1008 Figure A2. Comparison of spectra obtained from SCOPE model inversion and image average
1009 spectra for one monitored tree per treatment: Control (a), RDI1 (b) and RDI2 (c).

1010